

Shaping chaos in bilayer graphene cavities

Jucheng Lin,^{1,2,3,*} Yicheng Zhuang,^{1,2,4,*} Anton M. Graf,^{1,2,5} Joonas Keski-Rahkonen,^{1,2} and Eric J. Heller^{1,2}

¹*Department of Chemistry and Chemical Biology,
Harvard University, Cambridge, Massachusetts 02138, USA*

²*Department of Physics, Harvard University, Cambridge, Massachusetts 02138, USA*

³*School of Physics and Astronomy, Shanghai Jiao Tong University, Shanghai 200240, China*

⁴*School of Physics, Peking University, Beijing 100871, China*

⁵*Harvard John A. Paulson School of Engineering and Applied Sciences,
Harvard, Cambridge, Massachusetts 02138, USA*

(Dated: January 5, 2026)

Bilayer graphene cavities where electrons are confined within finite graphene flakes provide an alluring platform not only for the future nanoelectronic devices owing to the tunable energy gap but also for investigating the quantum nature of chaos due to the trigonal warping of their Fermi surface. Here we demonstrate that rotating the cavity boundary relative to the underlying lattice structure drives a quantum transition from nearly integrable dynamics to chaotic regime, observed as a concomitant crossover of eigenvalue statistics and eigenstate profiles. Complementing the full quantum treatment, we examine the classical backbone of this onset of chaos by employing semiclassical ray dynamics. Our results position bilayer graphene cavities as a promising venue for investigating and engineering quantum-chaotic behavior in graphene-based devices.

I. INTRODUCTION

Most physical systems are nonintegrable and can exhibit chaotic behavior in their classical limit [1]. The huge qualitative differences in integrable and chaotic behavior can be pivotal to the function of quantum devices. Billiard models have long served as canonical model systems for studying such behavior, in which dynamical complexity arises solely from the geometry of the confining boundary [2]. In the quantum regime, billiards correspond to idealized cavities governed by the Schrödinger equation with boundary conditions encoding information on the underlying classical motion, thereby providing a direct window into the quantum signatures of chaos [3–9]. This paradigm have played an essential role to establish the semiclassical link between chaotic classical dynamics and quantum features, leading the way towards the random matrix theory [10] as a general organizing principle for chaotic quantum systems, further culminating in the Bohigas–Giannoni–Schmit [11] and Berry [12] conjectures. Consequently, billiard systems have become a foundational testbed for various quantum-chaotic phenomena [3–9], ranging from the universality of level statistics and their periodic-orbit corrections to wavefunction ergodicity and its notable exceptions, such as quantum scarring.

Nearly all of the aforementioned results are rooted in the Schrödinger dynamics with an isotropic quadratic dispersion, as commonly realized in semiconductor quantum wells acting as soft-wall billiards [9]. However, not all quantum devices obey the Schrödinger equation; some of them obey the Dirac equation. A distinct class of billiards arises for relativistic wave equations with linear

dispersion, first exemplified by the neutrino billiard of Berry and Mondragon [13]. On the other hand, low-energy quasiparticles in a monolayer graphene (MLG) cavity emulate the physics of the Dirac equation [14–16], in which pseudospin, valley degrees of freedom, and relativistic boundary conditions fundamentally modify the correspondence between classical dynamics and quantum properties. As a result of being more accessible than a hypothetical neutrino billiard, an extensive amount of investigations has focused on MLG devices to examine the characteristics of a pseudo-relativistic quantum system, such as Klein tunneling [17], the creation and probing of whispering gallery mode resonators [18], spectral statistics and wavefunction properties [19–21] and recently the direct visualization of relativistic quantum scars [22].

Beyond the extensive interest in MLG [23–25], bilayer graphene (BLG) has emerged as a highly versatile platform in its own right [26]. Recent advances have demonstrated exceptional material quality and electrostatic control [27, 28], together with a wealth of novel physical phenomena [29–35]. For example, an out-of-plane electric field induces a tunable band gap by breaking layer symmetry, enabling electrostatically defined confinement [26, 36–39]. Alternatively, the necessary confinement can be created through lithographic methods [see, e.g., Refs. [40–42]], where the BLG is either cut or grown into a flake of desired geometry, producing hard-wall confinement reminiscent of a quantum billiard. In contrast to MLG, BLG lacks relativistic Dirac dynamics at low energies but instead hosts distinct phenomena, including Zitterbewegung-like motion arising from interlayer coupling [43]. Even though the low-energy dispersion is quadratic, it is strongly modified by trigonal warping [26].

The pronounced role of trigonal warping in BLG has been demonstrated under a wide range of conditions [30, 31, 44–46], with scanning tunneling microscopy providing

* These authors contributed equally to this work.

quasi-direct access to its anisotropic Fermi surface. This anisotropy renders the electronic dynamics highly sensitive to electrostatic gating [47, 48] and strain [49], as well as to lattice orientation. Notably, gate tuning alone can induce a coexistence of regular and chaotic dynamics even in highly symmetric BLG quantum dots [50]. Compared to MLG and common two-dimensional electron gas structures, trigonal warping allows the semiclassical dynamics to be tuned with far greater flexibility. In fact, semiclassical ray-dynamics and Poincaré analyses have revealed phase-space structures and periodic-orbit stability properties that are qualitatively distinct from those of conventional billiards [50–52]. Furthermore, the same anisotropy underlies electron-optical effects such as Veselago lensing, underscoring the unusual transport properties of BLG cavities [53].

While the features of BLG have motivated investigation in transport and device physics [54, 55], the implications remain largely uncharted in the context of quantum chaos, furthermore almost entirely confined to semiclassical perspective. The quantum mechanical properties of BLG cavities, such as their eigenstate morphology, spectral statistics, and the extent to which the semiclassical features persist or break down at the quantum level, are essentially unknown. Addressing these issues is crucial for understanding BLG cavities not only as electron-optical devices [53] but also as a platform for systematically investigating quantum-chaotic phenomena in strongly anisotropic materials.

Here, we demonstrate that boundary–lattice misalignment within BLG cavities induces a transition from the near-integrability to chaos, reflected in both eigenvalue statistics and eigenstate anatomy, while semiclassical ray dynamics exposes the classical phase-space restructuring responsible for this behavior that aligns with the prior work by Hentschel and co-workers [51, 56]. In particular, we investigate the interplay of the discrete nature of the lattice and the cavity geometry, going beyond widely used continuum models, such as utilized in Ref. [52]. Taken all together, we present a step toward the systematic investigation and design of chaos in BLG-based devices.

II. MODEL

We investigate an AB-stacked BLG cavity with regular hexagonal geometry, in order to elucidate the influence of trigonal warping and lattice–boundary misalignment. More specifically, the electronic structure of this cavity is described by the standard Slonczewski–Weiss–McClure tight-binding Hamiltonian [26]:

$$\begin{aligned} \mathcal{H} = & \sum_{\langle i,j \rangle_{\text{intra}}} \gamma_0 c_i^\dagger c_j + \sum_{\langle B_1, A_2 \rangle} \gamma_1 c_{B_1}^\dagger c_{A_2} + \sum_{\langle A_1, B_2 \rangle} \gamma_3 c_{A_1}^\dagger c_{B_2} \\ & + \sum_{\langle A_1, A_2 \rangle} \gamma_4 c_{A_1}^\dagger c_{A_2} + \sum_{\langle B_1, B_2 \rangle} \gamma_4 c_{B_1}^\dagger c_{B_2} + \text{H.c.}, \quad (1) \end{aligned}$$

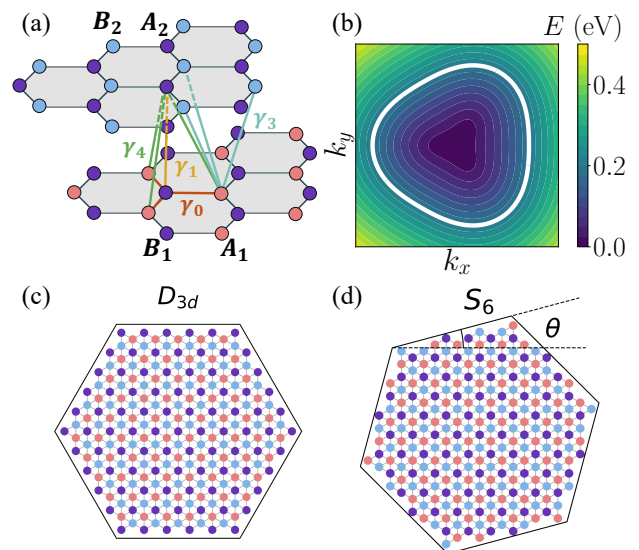


FIG. 1. Illustration of the tight-binding model, Fermi surface, and cavity geometry. (a) Schematic diagram of the BLG tight-binding model showing atoms and hopping. (b) K valley of BLG’s band structure, where the white curve represents the Fermi surface at $E = 0.2 \text{ eV}$, showing trigonal warping due to interlayer hopping γ_3 . (c) and (d) show diagrams of BLG cut into a hexagonal shape, where purple indicates the dimer atoms B_1 and A_2 , i.e., the vertically aligned sites that are directly coupled between the two layers, and red and blue indicate the non-dimer atoms A_1 and B_2 . In (c), the boundary is aligned with the inner lattice, and the point group of the atoms is D_{3d} . In (d), the boundary is rotated by 15° relative to the inner lattice, and the point group of the atoms is S_6 . The cavities we study contain millions of atoms.

which includes the dominant intralayer hopping γ_0 , the interlayer dimer coupling γ_1 , and the skew interlayer hoppings γ_3 and skew interlayer hopping between same-sublattice sites γ_4 . In the Hamiltonian above, c_i^\dagger (c_i) creates (annihilates) an electron on site i , and $\langle \cdot, \cdot \rangle$ denotes the corresponding in-plane or interlayer nearest-neighbor pairs as indicated in Fig. 1(a). Furthermore, A_1 and B_1 in Fig. 1(a) refer to the two sublattice atoms in the lower graphene layer, while A_2 and B_2 refer to the two sublattice atoms in the upper layer. Non-dimer sites in the top and bottom layers are shown in blue and red, respectively, while vertically aligned interlayer dimer sites are marked in purple.

The hopping parameters are chosen in accordance with established literature [26] (see *Materials and Methods* for details). Whereas dominant in-plane hopping γ_0 defines the Dirac-like dispersion within each layer and the vertical interlayer coupling γ_1 hybridizes the dimer sites ($B_1 - A_2$) yielding the characteristic low-energy parabolic bands, we are most interested in the skew parameter γ_3 which introduces trigonal warping and hence breaks the isotropy of the energy spectrum near the neutrality point. Fig. 1(b) shows a trigonally warped Fermi surface of BLG

stemming from the non-dimer coupling parametrized by γ_3 . Finally, same-sublattice interlayer hopping γ_4 couples A_1 - A_2 and B_1 - B_2 sites, lifting up electron-hole symmetry and only slightly modifying the band curvature.

We focus on the energy window $\Delta E = 0.18$ - 0.25 eV, where the Fermi surface exhibits pronounced trigonal warping. As displayed in Fig. 1(b), the K -valley Fermi surface becomes strongly anisotropic at energies a few hundred meV above the quadratic band-touching point. Within this energy window, the typical wavelength of a quantum state, $\lambda \approx 20$ nm, remains much larger than the lattice constant $a \approx 0.246$ nm. Moreover, the characteristic system size $L \approx 800$ nm $\gg \lambda$ places the studied system firmly in the semiclassical regime, justifying the semiclassical analysis employed below. Crucially, we have verified that both the numerical results and the corresponding conclusions below are qualitatively robust against variations in system size (the analysis is carried out in *Supplementary Material*).

To directly probe the interplay between the underlying and cavity boundary, we rotate the original hexagonal BLG cavity shown in Fig. 1(c) by an angle θ , as demonstrated in Fig. 1(d). However, the sixfold rotational symmetry of the lattice renders the atomic configuration 60° -periodic in the rotation angle θ . Furthermore, since the configurations at the angles θ and $60^\circ - \theta$ are equivalent, it is hence sufficient to restrict our consideration to the interval $0^\circ \leq \theta \leq 30^\circ$. The limiting cases 0° and 30° structurally correspond to boundary-aligned zigzag and armchair terminations, respectively; whereas intermediate angles produce misaligned edges with mixed zigzag-armchair character.

III. RESULTS

We compute eigenvalues and eigenstates of the Hamiltonian in (1) for the distinct angles $0^\circ \leq \theta \leq 30^\circ$, and then quantify the degree of chaos within the energy window ΔE . The simulation details are provided in *Materials and Methods* and *Supplementary Material*. However, before delving into these results, we briefly highlight two underlying key aspects about the chosen system.

First, we address the symmetry of the system (see *Materials and Methods* for details). In the case of the unrotated cavity ($\theta = 0$) shown in Fig. 1(c), the boundary is aligned with the crystalline axes, and the Hamiltonian respects the D_{3d} point-group symmetry, which further decomposes into the six irreducible representations A_{1g} , A_{2g} , A_{1u} , A_{2u} , E_g , and E_u . By contrast, for a representative rotated configuration ($\theta = 15^\circ$) presented in Fig. 1(d), the boundary orientation breaks the original mirror symmetries, downgrading the point group to S_6 , with four sectors A_g , A_u , E_g , and E_u .

Second, we note that a classical hexagonal billiard is an archetypal example of a pseudointegrable system [57, 58]: its interior angles are rational multiples of π , so trajectories evolve on higher-genus phase-space surfaces rather

than on invariant tori as in a fully integrable system. On the quantum side, such pseudointegrable billiards display hybrid spectral statistics, interpolating between regular and chaotic behavior, but are frequently characterized by the semi-Poisson distribution [58–63] (see also *Materials and Methods*). Our BLG cavity, however, differs from the idealized classical and quantum billiards due to the trigonal warping, and the discrete lattice which removes the sharp boundary corners causing classical pseudointegrable dynamics. Therefore, it is not a priori clear whether pseudointegrability carries over to our system. As we show next, the BLG cavity does inherit this feature to some degree, and we also explore its manifestation in the eigenfunction profiles that is a much less studied aspect compared to spectral statistics.

A. Level Statistics

We begin by estimating the degree of chaos in terms of the nearest-neighbor level spacing distribution and the spectral rigidity $\Delta_3(L)$ which are computed within each symmetry-resolved sector, probing the short- and long-range spectral correlations, respectively. Additional quantification is provided by the average gap ratio $\langle \tilde{r} \rangle$ and the average spectral rigidity $\langle \Delta_3 \rangle$. Figure. 2 summarizes these measures for the unrotated cavity and for a cavity rotated by $\theta = 15^\circ$. We further classify the (sub)spectra following the spirit of the Bohigas-Giannoni-Schmit conjecture [11]: a regular spectrum is associated with Poisson statistics, whereas a chaotic spectrum conform to the Gaussian Orthogonal Ensemble (GOE) or Gaussian Unitary Ensemble (GUE), depending on the presence or absence of time-reversal symmetry, respectively. The latter is also referred as Wigner-Dyson behavior. Our quantum-chaos estimations are detailed in *Materials and Methods*.

The unrotated hexagonal cavity exhibits a pronounced sector-to-sector separation: two one-dimensional sectors, A_{1u} and A_{2g} , are nearly uncorrelated (Poisson-like), whereas the remaining sectors display intermediate, semi-Poisson statistics characteristic of pseudointegrable polygonal billiards. This sector dependence reflects the different boundary constraints imposed by the symmetry projections, which can lead to distinct effective dynamics within the same device.

The Poisson-like behavior of the A_{1u} and A_{2g} sectors originates from a symmetry reduction of the boundary-value problem. In this sector, the parity constraints enforce nodal lines that act as effective Dirichlet boundaries, so the hexagon reduces to an equilateral-triangle fundamental domain. Since the equilateral triangle is integrable, this sector naturally exhibits near-Poisson statistics, consistent with the standard quantum billiard correspondence. Atomistic zigzag details do not change this large-scale geometry.

Fig. 2(a) shows the symmetry-resolved statistics for the unrotated cavity in the window 0.18 - 0.25 eV (2,978

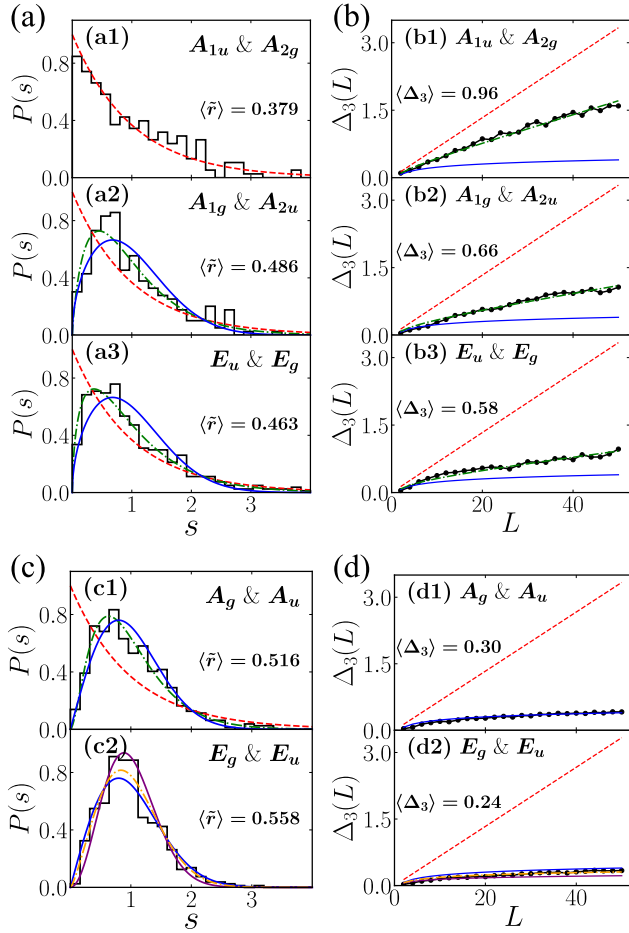


FIG. 2. Level Statistics of unrotated cavities and rotated BLG cavities. (a) and (b) show the level spacing statistics and spectral rigidity for the unrotated cavity, with the corresponding $\langle \tilde{r} \rangle$ values and averaged rigidity indicated in each panel. The red dashed line denotes the Poisson distribution, the blue solid line represents the Wigner–Dyson distribution, and the green dash-dotted line shows the fitted semi-Poisson distribution. (c) and (d) present the same analyses for the cavity rotated by 15° . The purple solid line represents the GUE distribution, and the orange dash-dotted line denotes the fitted GOE–GUE distribution.

levels). The A_{1u} and A_{2g} sectors yield the same value $\langle \tilde{r} \rangle = 0.379$, close to the Poisson limit, indicating a near-integrable channel. In contrast, the A_{1g} and A_{2u} sectors show stronger level repulsion with $\langle \tilde{r} \rangle = 0.486$, while the E_u and E_g sectors exhibit intermediate statistics with $\langle \tilde{r} \rangle = 0.463$. Both are well captured by semi-Poisson fits with $\beta = 0.83$ and 0.57 , respectively (see *Materials and Methods* for the fitting form). The corresponding rigidity curves in Fig. 2(b) follow the same hierarchy, but they appear slightly more Wigner–Dyson-like than suggested by $\langle \tilde{r} \rangle$. This kind of mismatch is common in the semi-Poisson-like intermediate regime, where short-range and long-range correlations can behave differently [64]. We further observe that the E sectors are

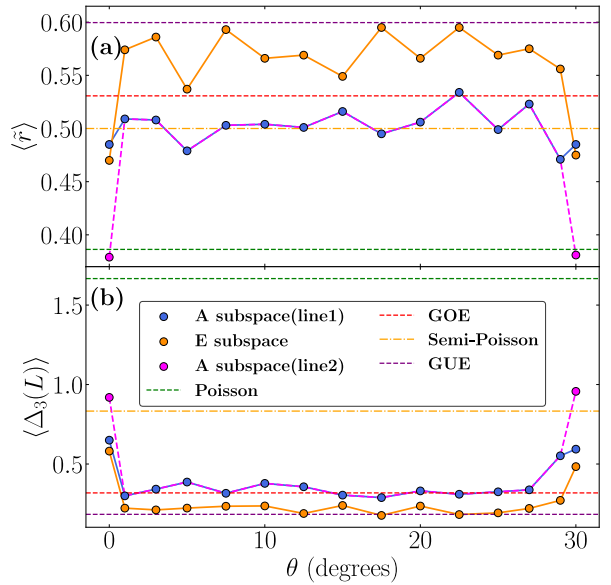


FIG. 3. Angle dependence of $\langle \tilde{r} \rangle$ and $\langle \Delta_3 \rangle$ on θ . (a) and (b) present the dependence of the r -value and the average spectral rigidity on the rotation angle θ for the A and E subspaces, respectively. In the A subspaces, two lines are shown: for the unrotated cases $\theta = 0^\circ$ and 30° , the blue solid line corresponds to the pseudointegrable sector, while the purple dashed line represents the integrable sector.

systematically more GUE-like than the A sectors, while the latter remain closer to GOE behavior, consistent with the fact that time-reversal invariance is lost within the E subspaces whereas the A subspaces remain time-reversal symmetric [65].

The rotated cavity shows a qualitatively different behavior. As illustrated by Fig. 2(c,d) for $\theta = 15^\circ$, the A sector remains intermediate with $\langle \tilde{r} \rangle = 0.516$, while the E sector shifts toward Wigner–Dyson correlations with $\langle \tilde{r} \rangle = 0.558$ and a strongly suppressed exponential tail. The data are well described by a mixed GOE–GUE interpolation [10] (see *Materials and Methods* for the fitting form), demonstrating that lattice–boundary misalignment removes the near-integrable channel present at $\theta = 0^\circ$ and drives the spectrum toward fully chaotic statistics. The rigidity shows a consistent trend: $\langle \Delta_3 \rangle$ decreases to 0.31 in A and 0.24 in E , approaching the GOE/GUE limits.

Fig. 3 summarizes the evolution with rotation angle. In the A sector, one branch remains in the intermediate (semi-Poisson-like) regime across all angles, while the branch that is Poisson-like at $\theta = 0^\circ$ and 30° rapidly increases toward Wigner–Dyson values as θ departs from these commensurate alignments. In the E sector, $\langle \tilde{r} \rangle$ increases more steadily and approaches the GOE/GUE range over a broad interval of angles. The averaged rigidity $\langle \Delta_3 \rangle$ exhibits the same overall trend, shown in Fig. 3(b), indicating that the enhancement of chaotic cor-

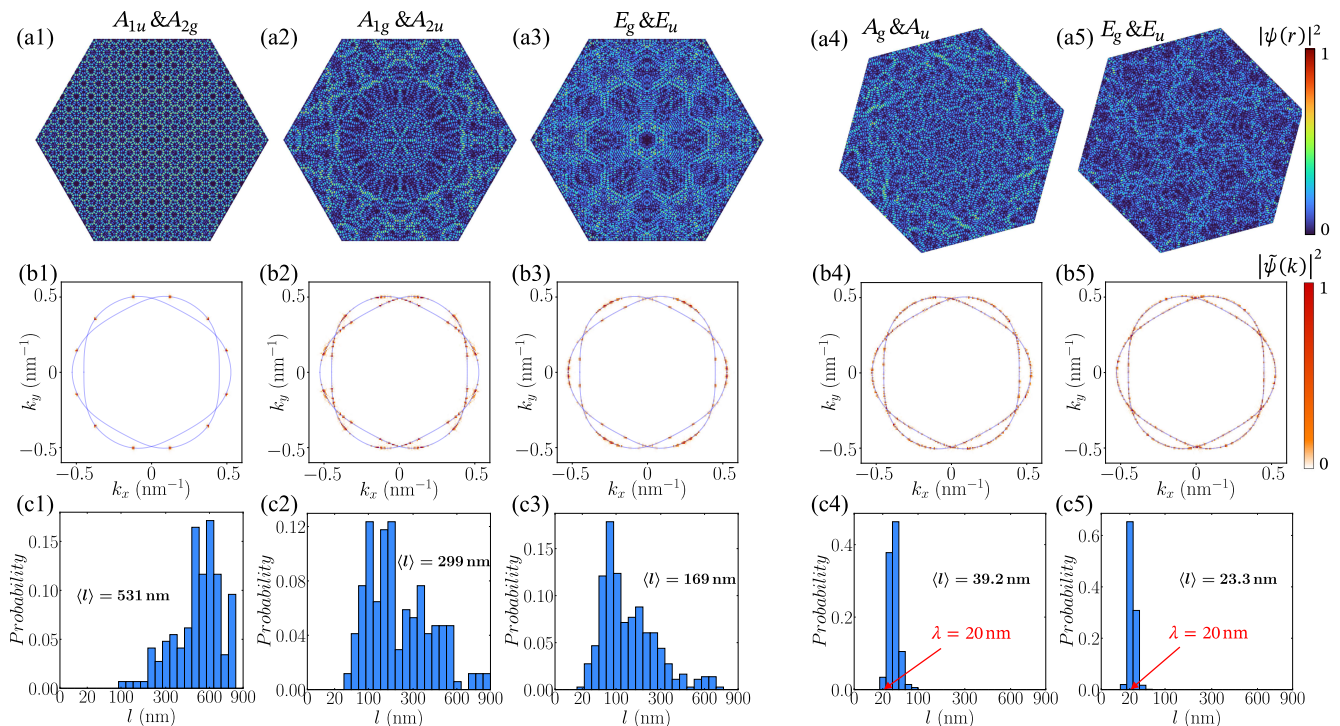


FIG. 4. The wavefunctions and their associated statistical properties. (a1)–(a3) representative probability density distributions $|\psi(\mathbf{r})|^2$ of eigenstates in unrotated cavities for different symmetry subspaces. (a4) and (a5) the corresponding results for the rotated case. (b1)–(b5) the associated distributions $|\tilde{\psi}(\mathbf{k})|^2$ in momentum space with trigonal warped Fermi surface at K and K' . (c1)–(c5) the statistical behavior of the correlation length l for the unrotated and rotated cavities across the symmetry subspaces.

relations is robust and does not require fine tuning of θ .

B. Eigenstates

To connect the spectral crossover to wavefunction structure, we study the eigenstates and quantify how lattice–boundary misalignment modifies their spatial correlations. The structure of eigenstates reflects the nature of the underlying classical dynamics. Integrable systems exhibit regular standing-wave patterns, whereas chaotic systems follow Berry’s random wave model and may host quantum scars associated with unstable classical orbits [10, 12, 66]. Pseudointegrable systems interpolate between these limits and often show symmetry-dependent eigenstate structures [63].

To quantify how rotation modifies the eigenstates, we characterize their spatial structure using an autocorrelation function, from which we extract a correlation length l as a measure of spatial coherence (see *Materials and Methods*). The correlation length l measures the typical length scale over which the wavefunction remains correlated: smaller l indicates more chaotic, spatially uncorrelated states, while larger l corresponds to more regular behavior. For a fully chaotic system, Berry’s random wave model predicts l to be equal to the wavelength λ

of the wavefunction [12]. In our system, $\lambda \approx 20$ nm at energies around 0.2 eV. We compute statistical averages of l from 1,056 eigenstates near this energy to assess the degree of chaos as a function of rotation angle.

We present representative eigenstates from each symmetry subspace in Fig. 4. The real-space probability density distributions are shown in Figs. 4(a1)–(a5), while the corresponding momentum-space structures, obtained from the Fourier transform $\tilde{\psi}(\mathbf{k}) = \int d^2\mathbf{r} e^{-i\mathbf{k}\cdot\mathbf{r}} \psi(\mathbf{r})$, are displayed in Figs. 4(b1)–(b5), together with the trigonal-warped Fermi surfaces in the K and K' valleys.

For the unrotated cavity, the A_{1u} and A_{2g} sectors exhibit regular standing-wave patterns (see Fig. 4(a1)), characteristic of integrable eigenstates [67]. Correspondingly, its momentum-space density is localized at discrete points on the Fermi surface (see Fig. 4(b1)), reflecting the dominance of a small number of plane-wave components. In contrast, eigenstates from the A_{1g} and A_{2u} , E_u and E_g sectors display more irregular spatial structures (see Figs. 4(a2),(a3)), accompanied by broader momentum-space distributions involving a larger set of wave vectors (see Figs. 4(b2),(b3)), consistent with their pseudointegrable nature.

Representative eigenstates from the rotated cavities, shown in Figs. 4(a4),(a5), exhibit highly irregular real-space density profiles without clear signatures of periodic orbits. Their momentum-space densities (see

Figs. 4(b4),(b5)) form nearly continuous distributions along the trigonal-warped Fermi surface, indicating random-wave-like behavior. Unlike Berry's random wave model with isotropic wave vectors, the randomness here arises from plane waves constrained to the warped Fermi surface.

The statistical analysis of the correlation length is summarized in Figs. 4(c1)–(c3). In the unrotated cavity, all symmetry subspaces yield average correlation lengths much larger than the wavelength $\lambda = 20$ nm, indicating the absence of full chaos. The integrable A_{1u} and A_{2g} sectors show the largest value, $\langle l \rangle = 531$ nm, while the pseudointegrable A_{1g} and A_{2u} , E_u and E_g sectors exhibit smaller values, $\langle l \rangle = 299$ nm and 169 nm, respectively, yet still significantly exceeding λ .

The change in the correlation length statistics upon rotation is striking. We consider a cavity rotated by $\theta = 15^\circ$, as shown in Figs. 4(c4) and (c5). For both the A and E sectors, the average correlation length decreases dramatically compared to the unrotated case, reaching $\langle l \rangle_A = 39.2$ nm and $\langle l \rangle_E = 23.3$ nm. Notably, in the E subspace, the correlation lengths of most eigenstates cluster around the wavelength $\lambda = 20$ nm, indicating the emergence of spatially uncorrelated, random-wave-like eigenstates.

The statistical behavior of the correlation length for a wider range of rotation angles is presented in the *Supplementary Material*. In addition, we analyze the momentum space distribution in *Supplementary Material*, which shows that rotation leads the wavefunctions to be composed of a larger number of plane waves with different wavevectors. These results indicate that rotation of the BLG cavity induces quantum chaos by significantly suppressing spatial correlations and increasing the number of contributing plane wave components for the eigenstates.

IV. SEMICLASSICAL DYNAMICS

To provide an intuitive dynamical picture of how trigonal warping reshapes the cavity behavior, we complement the tight-binding analysis with a simplified semiclassical ray model. Here, we isolate the geometric effects of the warped dispersion and the resulting anisotropic group velocity. We therefore adopt a continuum bulk description based on the standard four-band Hamiltonian for AB-stacked bilayer graphene [26], used here as a minimal description of warping-induced anisotropy in the bulk dispersion. This model intentionally omits atomistic edge details and serves as a heuristic tool for visualizing how lattice–boundary misalignment modifies the effective cavity dynamics.

In this framework, the cavity is modeled as an anisotropic Minkowski billiard [68]: rays propagate with the band velocity $\mathbf{v}(\mathbf{k}) = \nabla_{\mathbf{k}}E(\mathbf{k})$ along a warped constant-energy contour, and each boundary collision is implemented by enforcing conservation of energy and the tangential momentum component (see *Supplemen-*

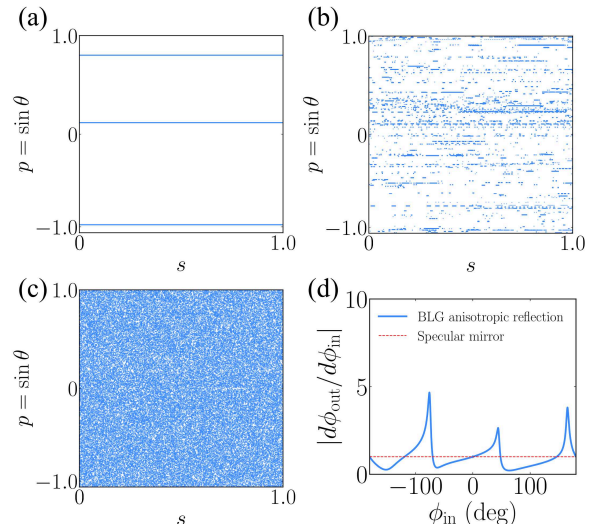


FIG. 5. Poincaré sections constructed by recording, for a single trajectory crossing a chosen reference edge, the boundary coordinate s (position along the edge) and the incidence angle θ (relative to the boundary normal). (a) With the boundary aligned to crystalline C_3 axis, the map collapses onto a few invariant curves characteristic of pseudo-integrable motion. (b) After rotating the cavity by 15° , the map spreads quasi-ergodically over the accessible phase space. (c) For comparison, a mirror reflecting irrational hexagon shows uniformly filled Poincaré points, demonstrating true ergodicity without crystalline commensurability. (d) The angular magnification $|d\phi_{\text{out}}/d\phi_{\text{in}}|$ for BLG's anisotropic reflection (blue) compared with the constant unit magnification of specular mirror reflection (red dashed). The variations in BLG magnification quantify the underlying warping responsible for the structures in Figs. 5 (a) and (b).

tary Material for the technical details).

Unlike geometric mirror reflection, this rule is momentum dependent and highly anisotropic. Nevertheless, because the warped Fermi contour remains strictly convex in our energy window, the resulting reflection map is smooth and area preserving. For polygonal billiards, the Lyapunov exponent is always zero. Because the boundary has no curvature and therefore cannot generate exponential separation of nearby trajectories. While certain polygons may be ergodic, they do not exhibit classical chaos. In our BLG ray-dynamics, trigonal warping introduces a momentum-dependent and highly anisotropic reflection rule. Although the angular magnification in Fig 5 (d) displays pronounced fluctuations and sharp peaks for specific incidence angles, our numerical evaluation still yields a maximal Lyapunov exponent $\lambda_{\text{max}} = 0$. Thus, trigonal warping does not generate exponential sensitivity in the semiclassical dynamics. However, $\lambda_{\text{max}} = 0$ does not mean that the dynamics is unchanged. As shown below, the anisotropic reflection map can strongly modify the ergodicity of the dynamics.

The Poincaré sections in Fig. 5 are constructed by

recording the arclength coordinate s and incidence angle θ whenever a ray intersects a fixed reference edge of the hexagon, over 5×10^5 collisions. When the boundary is aligned with a crystalline C_3 axis, the warped reflection rule is commensurate with the boundary symmetry. As a result, the warped reflection rule effectively reduces to ordinary specular reflection [50]. Successive reflections recur along a small set of preferred directions. Consecutive reflections therefore repeat only a small set of incidence angles, and the resulting Poincaré section collapses into a few discrete lines rather than filling the available phase space (see Fig. 5(a)). The motion is confined to these invariant lines, consistent with pseudo-integrable dynamics.

After rotating the cavity by 15° , this commensurability is lost. The warped reflection rule becomes incommensurate with the boundary, and incidence angles no longer recur coherently. The resulting Poincaré section displays a dense but structured phase-space pattern consistent with the quasi-ergodic regime discussed by Wang *et al* [69]: the trajectory becomes dense in phase space, but the point cloud remains pronounced non-uniform even after long evolution times. Compared to Fig. 5(c), bands of enhanced density and filamentary streaks persist across the section, and the occupancy of phase space shows clear variations in the coordinates (s, p) (see Fig. 5(b)). This slow, non-uniform phase-space filling provides a classical counterpart to the spectral crossover discussed above.

For comparison, Fig. 5(c) shows a mirror-reflecting irrational hexagon. The Poincaré points fill the allowed domain uniformly, demonstrating genuinely ergodic behavior. Compared to Fig. 5(b), the trajectory fills the phase space uniformly after only a short time.

V. DISCUSSION AND CONCLUSION

The emergence of quantum chaos upon misaligning the boundary and the lattice can be understood from a semiclassical perspective. We emphasize that the *chaos* here refers to quantum chaos, indicated by Wigner–Dyson spectral statistics and random wave eigenstates. Although we use a simplified semiclassical ray-dynamics construction, this model is intended to highlight the geometric consequences of the warped dispersion. No simple semiclassical description fully captures the atomistic boundary physics of the lattice model.

The simplified semiclassical picture nonetheless provides a meaningful interpretation of the observed transition. The rotated cavity exhibits quasi-ergodic phase space spreading, and such semiclassical ergodicity is known to be sufficient to generate Wigner–Dyson statistics even in the absence of strong classical chaos or positive Lyapunov exponents. Indeed, studies of non-hyperbolic systems, such as the quantum triangle map [69], triangular cavities [70], and parabolic triangle maps [71], have shown that classical quasi-ergodicity alone is sufficient to produce GOE or GUE level statistics in the

semiclassical limit, highlighting the role of classical mixing and ergodic properties in shaping quantum spectral behavior.

In addition, for a rotated BLG cavity defined on a lattice, one must distinguish geometric incommensurability from atomistic edge roughness. When the cavity is rotated relative to the underlying lattice, the boundary becomes a mixture of zigzag and armchair segments and develops kinks. Since mixed edges are known in MLG to modify intervalley scattering and consequently affect spectral correlations and eigenstate properties in specific cavity geometries [72, 73], one may worry that edge effects could play a dominant role in BLG. To assess the role of edge roughness, we perform two sets of control tests. First, we introduce artificial kinks on an unrotated hexagon and find that increasing the number of kinks leads to a slow increase of $\langle \tilde{r} \rangle$. Second, we rotate monolayer cavity, where trigonal warping is absent at low energies and the symmetry is reduced from D_6 to C_6 upon rotation. In MLG, $\langle \tilde{r} \rangle$ increases slightly, but the spectrum remains semi-Poisson even up to 10° (see *Supplementary Information*). This comparison indicates that edge roughness provides a gradual, angle-dependent contribution to the spectral correlations.

In BLG, by contrast, trigonal warping provides a much stronger mechanism that can drive a rapid transition. A rotation as small as 0.1° , corresponding to shifting the lattice by only one kink and producing negligible geometric deformation, is already sufficient to drive the spectrum to Wigner–Dyson statistics. At larger rotation angles, edge effects become progressively more important, since the increased armchair content enhances intervalley scattering and the semiclassical reflection rule is no longer expected to apply [74]. We therefore view the onset of quantum chaos in rotated BLG cavities as the combined outcome of (i) a dominant trigonal-warping mechanism that rapidly destroys the commensurability between the boundary and the bulk dynamics, and (ii) additional edge roughness effects that become increasingly relevant at larger rotation angles.

An important exception is the 30° , where the lattice and boundary become commensurate and edge physics becomes dominant. In this geometry, the spectrum shifts back toward quasi-integrable behavior. The boundary is closer to a uniform armchair termination, where intervalley physics is enhanced. Because our semiclassical model neglects atomistic edge conditions, its bulk-mismatch criterion is not expected to capture this edge-dominated symmetry restoration.

The BLG cavity model in our study can be experimentally realized. A hexagonal graphene cavity can be experimentally realized via CVD growth, and the rotated cavity model considered in our work corresponds to the hexagon with kinks [75]. In addition, such cavities can be obtained either by patterning BLG into discrete shapes, creating hard-wall confinement [14, 73, 76], or by using electrostatic gates to define a soft confinement potential, allowing tunable control over the dot occupancy and tun-

nel barriers [77–79]. Low temperature transport measurements, such as Coulomb blockade and excited state spectroscopy, can probe energy level statistics and wavefunction distributions, enabling experimental access to signatures of quantum chaotic behavior [80]. These approaches offer complementary ways to explore and control quantum chaos in BLG-based systems.

For future studies of BLG cavities, one can focus on controlling quantum behavior by tuning various parameters of the system. One promising direction is to introduce an external electric field, which can modify electron dynamics and selectively generate or tune specific wavefunction patterns. The interplay among the electric field, cavity geometry, and trigonal warping may give rise to a rich variety of dynamical regimes and quantum phenomena. In particular, it may enable the controlled manipulation of superscars in classically pseudointegrable cavities [81, 82]. Other factors, such as an applied magnetic field or an interlayer potential difference, can also be used to tune the system by altering its symmetry and internal electronic dynamics.

In conclusion, we have shown that misalignment between the BLG lattice and the hexagonal boundary fundamentally reshapes both the spectral and eigenstate properties of the cavity. Rotating the boundary removes the high symmetry subspaces in the unrotated cavity, produces Wigner–Dyson distribution of level spacing, and drives the eigenstates’ correlation lengths toward the wavelength scale, signaling the emergence of fully chaotic eigenstates. The semiclassical analysis confirms that this transition originates from the loss of commensurability between the warped Fermi surface and the polygonal boundary, which generates ergodicity in phase space and correspondingly causes quantum chaos. Overall, our results demonstrate that the boundary-lattice interplay provides an effective and experimentally accessible route for engineering and controlling quantum chaos in BLG cavities, with direct relevance to controllable electron transport in graphene and other mesoscopic systems [83–85].

VI. MATERIALS AND METHODS

A. Numerical implementation of eigenvalue and eigenstate simulations

All numerical simulations presented in this work are performed using the `pybinding` Python package, which provides a flexible and efficient framework for tight-binding modeling of two-dimensional materials [86]. Working with an atomistic tight-binding Hamiltonian on the physical honeycomb bilayer lattice avoids discretizing a continuum model on a Cartesian real-space grid, which can introduce artificial square-lattice (D_4) anisotropies that contaminate symmetry-sensitive spectral statistics [52]. For the same reason, our calculations do not suffer from spurious fermion-doubling artifacts associated with

finite-difference discretizations of continuum Dirac theories [87].

B. Tight-binding model parameters

For the tight-binding model of BLG, we adopt the commonly used parameters for AB-stacked layers. The lattice constant for BLG is $a = 0.246$ nm, and the interlayer distance is $d = 0.335$ nm. The intralayer nearest-neighbor hopping is $t_0 = 3.16$ eV, the interlayer vertical hopping between dimer sites is $t_1 = 0.381$ eV, and the skew interlayer hoppings are $t_3 = 0.38$ eV and $t_4 = 0.14$ eV [54].

The circumradius of the cavity is set to $r = 400$ nm that corresponds to a characteristic size $L \approx 800$ nm. In our numerical calculations, the hexagonal cavities contain on the order of 10^6 lattice sites, but we are able to resolve fully quantum spectrum in this regime where semi-classical or continuum approximations would commonly be applied.

C. Symmetry Analysis

The symmetry of the tight-binding Hamiltonian differs between the two configurations we study. When the boundary is aligned with the crystalline axes, the tight-binding Hamiltonian respects the full D_{3d} symmetry of the BLG lattice. This group contains a threefold rotation C_3 , inversion \mathcal{I} , and three vertical mirror operations σ_v .

Since $[\mathcal{H}, \mathcal{R}_{2\pi/3}] = 0$, the eigenstates of \mathcal{H} can be chosen as simultaneous eigenstates of the 120° rotation operator $\mathcal{R}_{2\pi/3}$, namely

$$\mathcal{R}_{2\pi/3}\psi_n^{(m)}(\mathbf{r}) = e^{i2\pi m/3}\psi_n^{(m)}(\mathbf{r}), \quad m = 0, \pm 1. \quad (2)$$

The rotation-invariant sector $m = 0$ further splits under inversion \mathcal{I} and mirror reflection σ_v into four one-dimensional irreducible representations. To make these parity properties explicit, we label the corresponding eigenstates as $\psi_n^{(0,p_i,p_\sigma)}$, where $p_i = \pm 1$ and $p_\sigma = \pm 1$ denote the eigenvalues under inversion and mirror operations, respectively:

$$\mathcal{I}\psi_n^{(0,p_i,p_\sigma)} = p_i\psi_n^{(0,p_i,p_\sigma)}, \quad \sigma_v\psi_n^{(0,p_i,p_\sigma)} = p_\sigma\psi_n^{(0,p_i,p_\sigma)} \quad (3)$$

In this notation, $(p_i, p_\sigma) = (+, +)$, $(+, -)$, $(-, +)$, and $(-, -)$ correspond to the irreducible representations A_{1g} , A_{2g} , A_{1u} , and A_{2u} , respectively. The correspondence between the eigenvalues of the symmetry operations (m , p_i , and p_σ) and the irreducible representations is summarized in Table I (left).

When the boundary is rotated by an angle θ , mirror symmetry is broken, and the symmetry group of the tight-binding Hamiltonian reduces to S_6 . The corresponding symmetry properties and irreducible representations are listed in Table I (right). Based on the

TABLE I. Symmetry sectors used for D_{3d} (left) and S_6 (right). Listed are the irreducible subspace's dimension, rotation sector m , and inversion/mirror parities p_i/p_σ .

Group	Irrep	Dim.	m	p_i	p_σ
D_{3d}	A_{1g}	1	0	+1	+1
	A_{2g}	1	0	+1	-1
	A_{1u}	1	0	-1	+1
	A_{2u}	1	0	-1	-1
	E_g	2	± 1	+1	0
	E_u	2	± 1	-1	0
Group	Irrep	Dim.	m	p_i	
S_6	A_g	1	0	+1	
	A_u	1	0	-1	
	E_g	2	± 1	+1	
	E_u	2	± 1	-1	

symmetry analysis, we can study the eigenstates independently in each subspace.

D. Level Statistics

To characterize the spectral properties for each orientation angle θ , we compute the ordered eigenvalues $\{E_i\}$ of the tight-binding Hamiltonian and analyze their fluctuations after unfolding. Nearest-neighbor spacings are defined as $s_i = E_{i+1} - E_i$, and the resulting spacing distribution $P(s)$ is compared with the standard Poisson and Wigner-Dyson forms of random-matrix theory [11]. We evaluate the ratio of consecutive spacings, $r_i = \frac{s_{i+1}}{s_i}$, $\tilde{r}_i = \min(r_i, 1/r_i)$, which takes the characteristic values $\langle \tilde{r} \rangle_P \simeq 0.386$, $\langle \tilde{r} \rangle_{\text{GOE}} \simeq 0.531$, and $\langle \tilde{r} \rangle_{\text{GUE}} \simeq 0.600$ [88].

Long-range correlations of spectrum are quantified using the spectral rigidity [89], which is defined as

$$\Delta_3(L) = \frac{1}{L} \min_{\{A,B\}} \int_E^{E+L} [N(E') - AE' - B]^2 dE' \quad (4)$$

where $N(E)$ is the unfolded staircase function. While integrable spectra show a linear increase of $\Delta_3(L)$ and chaotic spectra exhibit the logarithmic behavior predicted by random-matrix theory, the orientation-dependent evolution of Δ_3 provides a complementary measure of long-range correlations in BLG cavities. To quantify the degree of chaos in the system, we compute the index $\langle \Delta_3(L) \rangle$, defined as the average of $\Delta_3(L)$ over the range $L \in [10, 40]$. For reference, the typical values of $\langle \Delta_3 \rangle$ in the three limiting cases are approximately $\langle \Delta_3 \rangle_{\text{Poisson}} \simeq 1.67$, $\langle \Delta_3 \rangle_{\text{GOE}} \simeq 0.319$, and $\langle \Delta_3 \rangle_{\text{GUE}} \simeq 0.184$.

For comparison, we fit the level spacing distribution between Poisson and GOE taking the semi-Poisson form [64, 90, 91]

$$P_{\text{SP}}(\beta, s) = A_\beta s^\beta \exp[-(\beta + 1)s], \quad A_\beta = \frac{(\beta + 1)^{\beta+1}}{\Gamma(\beta + 1)}. \quad (5)$$

We also fit the level spacing distribution between GOE and GUE taking the form [10]

$$P_{\text{WD}}(\gamma, s) = a_\gamma s^\gamma \exp(-b_\gamma s^2), \quad (6)$$

where we have defined

$$b_\gamma = \left[\frac{\Gamma(\frac{\gamma+2}{2})}{\Gamma(\frac{\gamma+1}{2})} \right]^2 \quad \text{and} \quad a_\gamma = \frac{2b_\gamma^{(\gamma+1)/2}}{\Gamma(\frac{\gamma+1}{2})}. \quad (7)$$

with $\gamma = 1$ and $\gamma = 2$ correspond to GOE and GUE, respectively.

E. Correlation function analysis

To quantify how rotation influences the overall structure of the system's eigenstates, we analyze the two-point correlation function,

$$C(\mathbf{r}, \mathbf{r}') = \langle \psi^*(\mathbf{r})\psi(\mathbf{r}') \rangle. \quad (8)$$

According to Berry's random wave model for chaotic cavities, the wave function can be modeled as a superposition of plane waves with random phases and a fixed wavenumber k , $\psi(\mathbf{r}) = \sum_{n=1}^N a_n e^{i\mathbf{k}_n \cdot \mathbf{r}}$. After ensemble averaging, the correlation function becomes isotropic and depends only on the separation $r = |\mathbf{r} - \mathbf{r}'|$, taking the universal form

$$C(r) = J_0(kr), \quad (9)$$

where J_0 is the zeroth-order Bessel function of the first kind [12].

In contrast, in our model the correlation function is generally anisotropic and depends on both the magnitude and direction of the separation vector. To extract a scalar measure from the anisotropic correlation function, we define

$$C(r) \equiv \langle \max_{\hat{\mathbf{r}}'} C(\boldsymbol{\rho}, \boldsymbol{\rho} + \mathbf{r}') \rangle_{\boldsymbol{\rho}}, \quad |\mathbf{r}'| = r, \quad (10)$$

where the maximization is performed over all directions $\hat{\mathbf{r}}' = \mathbf{r}'/|\mathbf{r}'|$ of the displacement vector \mathbf{r}' , for a fixed separation $|\mathbf{r}'| = r$, and $\langle \dots \rangle_{\boldsymbol{\rho}}$ denotes an average over initial positions $\boldsymbol{\rho}$. We analyze the resulting correlation function by fitting it to the form

$$C(r) = J_0\left(2\pi \frac{r}{l}\right), \quad (11)$$

where l defines a correlation length that characterizes the spatial correlations of the eigenstates. We emphasize that the correlation length is used here as a relative and heuristic measure of spatial correlations. For a fully chaotic system, the correlation length reduces to the wavelength λ of the eigenfunction.

F. Semiclassical ray-dynamics

Direct time-stepping ray propagation in polygonal billiards with anisotropic dispersion is prone to numerical issues near grazing incidence and near vertices, where

corner sensitivity can lead to trajectory-dependent ambiguities. To obtain stable long-time dynamics, we implement the semiclassical motion as a discrete map between successive boundary collisions. We tabulate the relation between the incidence angle φ_{in} and the outgoing angle φ_{out} , determined by the conservation of energy and the tangential component k_t . Each table contains about 3×10^5 sampled angles. This approach encodes the warped reflection law once and for all, and removes the need to solve for φ_{out} by conducting a local root search at every collision.

Between collisions, the next collision point is found by ray-boundary intersection. The dynamics is thus an alternation of (i) intersection updates for free flight and (ii) table-based updates for reflection. This map-based

scheme maintains high angular accuracy even for nearly grazing trajectories and avoids artificial corner sticking and other corner-related numerical artifacts. As a result, we can compute long trajectories and Poincaré sections robustly.

ACKNOWLEDGMENTS

This project was supported by the National Science Foundation (Grant No. 2403491). We are thankful for the useful discussions with E. Räsänen, A. M. Bozkur, and J. Velasco Jr. A.M.G. thanks the Studienstiftung des Deutschen Volkes for financial support.

-
- [1] E. Ott, *Chaos in Dynamical Systems* (Cambridge University Press, 2002).
 - [2] N. Chernov and R. Markarian, *Chaotic Billiards*, Mathematical surveys and monographs (American Mathematical Society, 2006).
 - [3] H.-J. Stöckmann, *Quantum Chaos: An Introduction* (Cambridge University Press, 1999).
 - [4] E. J. Heller, *The Semiclassical Way to Dynamics and Spectroscopy* (Princeton University Press, 2018).
 - [5] M. Gutzwiller, *Chaos in Classical and Quantum Mechanics*, Interdisciplinary Applied Mathematics (Springer New York, 1991).
 - [6] F. Haake, *Quantum Signatures of Chaos*, Springer series in synergetics (Springer-Verlag, 1991).
 - [7] M. Tabor, *Chaos and integrability in nonlinear dynamics*, Vol. 3 (Wiley New York, 1989).
 - [8] G. Casati and B. Chirikov, *Quantum Chaos: Between Order and Disorder* (Cambridge University Press, 1995).
 - [9] K. Nakamura and T. Harayama, *Quantum Chaos and Quantum Dots*, Mesoscopic physics and nanotechnology (Oxford University Press, 2004).
 - [10] M. Mehta, *Random Matrices*, 3rd ed., Pure and Applied Mathematics (Academic Press, 2004).
 - [11] O. Bohigas, M. J. Giannoni, and C. Schmit, Characterization of chaotic quantum spectra and universality of level fluctuation laws, *Phys. Rev. Lett.* **52**, 1 (1984).
 - [12] M. V. Berry, Regular and irregular semiclassical wavefunctions, *J. Phys. A: Math. Gen.* **10**, 2083 (1977).
 - [13] M. V. Berry and R. J. Mondragon, Neutrino billiards: time-reversal symmetry-breaking without magnetic fields, *Proc. Royal Soc. London. A. Math. Phys. Sci.* **412**, 53 (1987).
 - [14] L. A. Ponomarenko, F. Schedin, M. I. Katsnelson, R. Yang, E. W. Hill, K. S. Novoselov, and A. K. Geim, Chaotic dirac billiard in graphene quantum dots, *Science* **320**, 356 (2008).
 - [15] D. Condado and E. Sadurní, An exactly solvable tight-binding billiard in graphene (2025), arXiv:2502.06092 [quant-ph].
 - [16] L. Huang, H.-Y. Xu, C. Grebogi, and Y.-C. Lai, Relativistic quantum chaos, *Phys. Reports* **753**, 1 (2018).
 - [17] C. W. J. Beenakker, Colloquium: Andreev reflection and klein tunneling in graphene, *Rev. Mod. Phys.* **80**, 1337 (2008).
 - [18] Y. Zhao, J. Wyrick, F. D. Natterer, J. F. Rodriguez-Nieva, C. Lewandowski, K. Watanabe, T. Taniguchi, L. S. Levitov, N. B. Zhitenev, and J. A. Stroscio, Creating and probing electron whispering-gallery modes in graphene, *Science* **348**, 672 (2015).
 - [19] A. K. Geim and K. S. Novoselov, The rise of graphene, *Nat. Mater.* **6**, 183 (2007).
 - [20] A. H. Castro Neto, F. Guinea, N. M. R. Peres, K. S. Novoselov, and A. K. Geim, The electronic properties of graphene, *Rev. Mod. Phys.* **81**, 109 (2009).
 - [21] A. R. Akhmerov and C. W. J. Beenakker, Boundary conditions for dirac fermions on a terminated honeycomb lattice, *Phys. Rev. B* **77**, 085423 (2008).
 - [22] Z. Ge, A. M. Graf, J. Keski-Rahkonen, S. Slizovskiy, P. Polizogopoulos, T. Taniguchi, K. Watanabe, R. Van Haren, D. Lederman, V. I. Fal'ko, E. J. Heller, and J. Velasco, Direct visualization of relativistic quantum scars in graphene quantum dots, *Nature* **635**, 841 (2024).
 - [23] A. H. Castro Neto, F. Guinea, N. M. R. Peres, K. S. Novoselov, and A. K. Geim, The electronic properties of graphene, *Rev. Mod. Phys.* **81**, 109 (2009).
 - [24] S. Das Sarma, S. Adam, E. H. Hwang, and E. Rossi, Electronic transport in two-dimensional graphene, *Rev. Mod. Phys.* **83**, 407 (2011).
 - [25] D. N. Basov, M. M. Fogler, A. Lanzara, F. Wang, and Y. Zhang, Colloquium: Graphene spectroscopy, *Rev. Mod. Phys.* **86**, 959 (2014).
 - [26] E. McCann and M. Koshino, The electronic properties of bilayer graphene, *Reports on Prog. Phys.* **76**, 056503 (2013).
 - [27] C. Tong, R. Garreis, A. Knothe, M. Eich, A. Sacchi, K. Watanabe, T. Taniguchi, V. Fal'ko, T. Ihn, K. Ensslin, *et al.*, Tunable valley splitting and bipolar operation in graphene quantum dots, *Nano Lett.* **21**, 1068 (2021).
 - [28] L. Banszerus, A. Rothstein, T. Fabian, S. Moller, E. Icking, S. Trellenkamp, F. Lentz, D. Neumaier, K. Watanabe, T. Taniguchi, *et al.*, Electron-hole crossover in gate-controlled bilayer graphene quantum dots, *Nano Lett.* **20**, 7709 (2020).
 - [29] L. Banszerus, K. Hecker, S. Möller, E. Icking, K. Watanabe, T. Taniguchi, C. Volk, and C. Stampfer, Spin re-

- laxation in a single-electron graphene quantum dot, *Nat. Commun.* **13**, 3637 (2022).
- [30] R. Garreis, A. Knothe, C. Tong, M. Eich, C. Gold, K. Watanabe, T. Taniguchi, V. Fal'ko, T. Ihn, K. Ensslin, and A. Kurzmann, Shell filling and trigonal warping in graphene quantum dots, *Phys. Rev. Lett.* **126**, 147703 (2021).
- [31] R. Garreis, C. Tong, J. Terle, M. J. Ruckriegel, J. D. Gerber, L. M. Gächter, K. Watanabe, T. Taniguchi, T. Ihn, K. Ensslin, *et al.*, Long-lived valley states in bilayer graphene quantum dots, *Nat. Phys.* **20**, 428 (2024).
- [32] R. Garreis, J. D. Gerber, V. Stará, C. Tong, C. Gold, M. Rösli, K. Watanabe, T. Taniguchi, K. Ensslin, T. Ihn, *et al.*, Counting statistics of single electron transport in bilayer graphene quantum dots, *Phys. Rev. Res.* **5**, 013042 (2023).
- [33] A. Kurzmann, Y. Kleedorin, C. Tong, R. Garreis, A. Knothe, M. Eich, C. Mittag, C. Gold, F. K. de Vries, K. Watanabe, *et al.*, Kondo effect and spin-orbit coupling in graphene quantum dots, *Nat. Commun.* **12**, 6004 (2021).
- [34] A. Kurzmann, M. Eich, H. Overweg, M. Mangold, F. Herman, P. Rickhaus, R. Pisoni, Y. Lee, R. Garreis, C. Tong, *et al.*, Excited states in bilayer graphene quantum dots, *Phys. Rev. Lett.* **123**, 026803 (2019).
- [35] C. Tong, F. Ginzler, A. Kurzmann, R. Garreis, L. Oostertag, J. D. Gerber, W. W. Huang, K. Watanabe, T. Taniguchi, G. Burkard, J. Danon, T. Ihn, and K. Ensslin, Three-carrier spin blockade and coupling in bilayer graphene double quantum dots, *Phys. Rev. Lett.* **133**, 017001 (2024).
- [36] E. McCann and V. I. Fal'ko, Landau-level degeneracy and quantum hall effect in a graphite bilayer, *Phys. Rev. Lett.* **96**, 086805 (2006).
- [37] H. Min, B. Sahu, S. K. Banerjee, and A. H. MacDonald, Ab initio theory of gate induced gaps in graphene bilayers, *Phys. Rev. B* **75**, 155115 (2007).
- [38] E. V. Castro, K. S. Novoselov, S. V. Morozov, N. M. R. Peres, J. M. B. L. dos Santos, J. Nilsson, F. Guinea, A. K. Geim, and A. H. C. Neto, Biased bilayer graphene: Semiconductor with a gap tunable by the electric field effect, *Phys. Rev. Lett.* **99**, 216802 (2007).
- [39] Y. Zhang, T.-T. Tang, C. Girit, Z. Hao, M. C. Martin, A. Zettl, M. F. Crommie, Y. R. Shen, and F. Wang, Direct observation of a widely tunable bandgap in bilayer graphene, *Nature* **459**, 820 (2009).
- [40] D. C. Bell, M. C. Lemme, L. A. Stern, J. R. Williams, and C. M. Marcus, Precision cutting and patterning of graphene with helium ions, *Nanotechnology* **20**, 455301 (2009).
- [41] C. Cong, T. Yu, Z. Ni, L. Liu, Z. Shen, and W. Huang, Fabrication of graphene nanodisk arrays using nanosphere lithography, *J. Phys. Chem. C* **113**, 6529 (2009).
- [42] C. Rubio-Verdú, G. Sáenz-Arce, J. Martínez-Asencio, D. Milan, M. Moaied, J. Palacios, M. J. Caturla, and C. Untiedt, Graphene flakes obtained by local electrofoliation of graphite with a stm tip, *Phys. Chem. Chem. Phys.* **19**, 8061 (2017).
- [43] R. Bao, L. Huang, Y.-C. Lai, and C. Grebogi, Conductance fluctuations in chaotic bilayer graphene quantum dots, *Phys. Rev. E* **92**, 012918 (2015).
- [44] C. Gold, A. Knothe, A. Kurzmann, A. Garcia-Ruiz, K. Watanabe, T. Taniguchi, V. Fal'ko, K. Ensslin, and T. Ihn, Coherent jetting from a gate-defined channel in bilayer graphene, *Phys. Rev. Lett.* **127**, 046801 (2021).
- [45] K. Kechedzhi, V. I. Fal'ko, E. McCann, and B. L. Altshuler, Influence of trigonal warping on interference effects in bilayer graphene, *Phys. Rev. Lett.* **98**, 176806 (2007).
- [46] V. Kaladzhyan, F. Joucken, Z. Ge, E. A. Quezada-Lopez, T. Taniguchi, K. Watanabe, J. Velasco, and C. Bena, Quasiparticle interference patterns in bilayer graphene with trigonal warping, *Phys. Rev. B* **104**, 235425 (2021).
- [47] T. Ohta, A. Bostwick, T. Seyller, K. Horn, and E. Rotenberg, Controlling the electronic structure of bilayer graphene, *Science* **313**, 951 (2006).
- [48] J. B. Oostinga, H. B. Heersche, X. Liu, A. F. Morpurgo, and L. M. Vandersypen, Gate-induced insulating state in bilayer graphene devices, *Nat. Mater.* **7**, 151 (2008).
- [49] M. Mucha-Kruczyński, I. L. Aleiner, and V. I. Fal'ko, Strained bilayer graphene: Band structure topology and Landau level spectrum, *Phys. Rev. B* **84**, 041404 (2011).
- [50] L. Seemann, A. Knothe, and M. Hentschel, Gate-tunable regular and chaotic electron dynamics in ballistic bilayer graphene cavities, *Phys. Rev. B* **107**, 205404 (2023).
- [51] L. Seemann, J. Lukin, M. Häckler, S. Gemming, and M. Hentschel, Complex dynamics in circular and deformed bilayer graphene-inspired billiards with anisotropy and strain, *Symmetry* **17** (2025).
- [52] F. Schoeppl, A. Mrenca-Kolasinska, M.-H. Liu, K. Schwarzmaier, K. Richter, and A. Knothe, Anisotropic transport in ballistic bilayer graphene cavities (2025), arXiv:2512.08588 [cond-mat.mes-hall].
- [53] V. V. Cheianov, V. Fal'ko, and B. L. Altshuler, The focusing of electron flow and a veselago lens in graphene p-n junctions, *Science* **315**, 1252 (2007).
- [54] J. W. González, H. Santos, M. Pacheco, L. Chico, and L. Brey, Electronic transport through bilayer graphene flakes, *Phys. Rev. B* **81**, 195406 (2010).
- [55] P. San-Jose, R. V. Gorbachev, A. K. Geim, K. S. Novoselov, and F. Guinea, Stacking boundaries and transport in bilayer graphene, *Nano Lett.* **14**, 2052 (2014).
- [56] M. Hentschel, S. Schlötzer, and L. Seemann, Ray-wave correspondence in anisotropic mesoscopic billiards, *Entropy* **27** (2025).
- [57] P. Richens and M. Berry, Pseudointegrable systems in classical and quantum mechanics, *Phys. D: Nonlinear Phenom.* **2**, 495 (1981).
- [58] Č. Lozej and E. Bogomolny, Intermediate spectral statistics of rational triangular quantum billiards, *Phys. Rev. E* **110**, 024213 (2024).
- [59] M. V. Berry and M. Robnik, Semiclassical level spacings when regular and chaotic orbits coexist, *J. Phys. A: Math. Gen.* **17**, 2413 (1984).
- [60] T. Cheon and T. D. Cohen, Quantum level statistics of pseudointegrable billiards, *Phys. Rev. Lett.* **62**, 2769 (1989).
- [61] E. B. Bogomolny, U. Gerland, and C. Schmit, Models of intermediate spectral statistics, *Phys. Rev. E* **59**, R1315 (1999).
- [62] O. Giraud, J. Marklof, and S. O'Keefe, Intermediate statistics in quantum maps, *J. Phys. A: Math. Gen.* **37**, L303 (2004).
- [63] D. Biswas and S. R. Jain, Quantum description of a pseudointegrable system: The $\pi/3$ -rhombus billiard, *Phys. Rev. A* **42**, 3170 (1990).

- [64] E. Bogomolny, U. Gerland, and C. Schmit, Short-range plasma model for intermediate spectral statistics, *The Eur. Phys. J. B* **19**, 121–132 (2001).
- [65] T. A. Lima, R. B. do Carmo, K. Terto, and F. M. de Aguiar, Time-reversal-invariant hexagonal billiards with a point symmetry, *Phys. Rev. E* **104**, 064211 (2021).
- [66] E. J. Heller, Bound-state eigenfunctions of classically chaotic hamiltonian systems: Scars of periodic orbits, *Phys. Rev. Lett.* **53**, 1515 (1984).
- [67] M. V. Berry, Regularity and chaos in classical mechanics, illustrated by three deformations of a circular ‘billiard’, *Eur. J. Phys.* **2**, 91 (1981).
- [68] E. Gutkin and S. Tabachnikov, Billiards in finsler and minkowski geometries, *J. Geom. Phys.* **40**, 277 (2002).
- [69] J. Wang, G. Benenti, G. Casati, and W.-g. Wang, Statistical and dynamical properties of the quantum triangle map, *J. Phys. A: Math. Theor.* **55**, 234002 (2022).
- [70] Č. Lozej, G. Casati, and T. Prosen, Quantum chaos in triangular billiards, *Phys. Rev. Res.* **4**, 013138 (2022).
- [71] M. Degli Esposti, S. O’Keefe, and B. Winn, A semi-classical study of the casati–prosen triangle map, *Nonlinearity* **18**, 1073 (2005).
- [72] P. Yu, Z.-Y. Li, H.-Y. Xu, L. Huang, B. Dietz, C. Grebogi, and Y.-C. Lai, Gaussian orthogonal ensemble statistics in graphene billiards with the shape of classically integrable billiards, *Phys. Rev. E* **94**, 062214 (2016).
- [73] I. Hagymási, P. Vancsó, A. Pálkás, and Z. Osváth, Interaction effects in a chaotic graphene quantum billiard, *Phys. Rev. B* **95**, 075123 (2017).
- [74] J. Wurm, K. Richter, and i. d. I. m. c. Adagideli, Edge effects in graphene nanostructures: From multiple reflection expansion to density of states, *Phys. Rev. B* **84**, 075468 (2011).
- [75] T. Ma, W. Ren, X. Zhang, Z. Liu, Y. Gao, L.-C. Yin, X.-L. Ma, F. Ding, and H.-M. Cheng, Edge-controlled growth and kinetics of single-crystal graphene domains by chemical vapor deposition, *Proc. Natl. Acad. Sci.* **110**, 20386 (2013).
- [76] A. Barreiro, H. S. J. van der Zant, and L. M. K. Vandersypen, Quantum dots at room temperature carved out from few-layer graphene, *Nano Lett.* **12**, 6096 (2012).
- [77] D. Subramaniam, F. Libisch, Y. Li, C. Pauly, V. Geringer, R. Reiter, T. Mashoff, M. Liebmann, J. Burgdörfer, C. Busse, T. Michely, R. Mazzarello, M. Pratzner, and M. Morgenstern, Wave-function mapping of graphene quantum dots with soft confinement, *Phys. Rev. Lett.* **108**, 046801 (2012).
- [78] A. S. M. Goossens, S. C. M. Driessen, T. A. Baart, K. Watanabe, T. Taniguchi, and L. M. K. Vandersypen, Gate-defined confinement in bilayer graphene-hexagonal boron nitride hybrid devices, *Nano Lett.* **12**, 4656 (2012).
- [79] A. Kurzman, H. Overweg, M. Eich, A. Pally, P. Rickhaus, R. Pisoni, Y. Lee, K. Watanabe, T. Taniguchi, T. Ihn, and K. Ensslin, Charge detection in gate-defined bilayer graphene quantum dots, *Nano Lett.* **19**, 5216 (2019).
- [80] L. Banszerus, S. Möller, E. Icking, K. Watanabe, T. Taniguchi, C. Volk, and C. Stampfer, Single-electron double quantum dots in bilayer graphene, *Nano Lett.* **20**, 2005 (2020).
- [81] E. Bogomolny and C. Schmit, Structure of wave functions of pseudointegrable billiards, *Phys. Rev. Lett.* **92**, 244102 (2004).
- [82] E. Bogomolny, B. Dietz, T. Friedrich, M. Miski-Oglu, A. Richter, F. Schäfer, and C. Schmit, First experimental observation of superscars in a pseudointegrable barrier billiard, *Phys. Rev. Lett.* **97**, 254102 (2006).
- [83] J. Velasco, L. Jing, W. Bao, Y. Lee, P. Kratz, V. Aji, M. Bockrath, C. N. Lau, C. Varma, R. Stillwell, D. Smirnov, F. Zhang, J. Jung, and A. H. MacDonald, Transport spectroscopy of symmetry-broken insulating states in bilayer graphene, *Nat. Nanotechnol.* **7**, 156–160 (2012).
- [84] H. Cao and J. Wiersig, Dielectric microcavities: Model systems for wave chaos and non-hermitian physics, *Rev. Mod. Phys.* **87**, 61 (2015).
- [85] R. Bao, L. Huang, Y.-C. Lai, and C. Grebogi, Conductance fluctuations in chaotic bilayer graphene quantum dots, *Phys. Rev. E* **92**, 012918 (2015).
- [86] D. Moldovan, M. Andelković, and F. Peeters, pybinding v0. 9.4: a python package for tight-binding calculations, Zenodo (2020).
- [87] H. Nielsen and M. Ninomiya, Absence of neutrinos on a lattice: (i). proof by homotopy theory, *Nucl. Phys. B* **185**, 20 (1981).
- [88] Y. Y. Atas, E. Bogomolny, O. Giraud, and G. Roux, Distribution of the ratio of consecutive level spacings in random matrix ensembles, *Phys. Rev. Lett.* **110**, 084101 (2013).
- [89] F. J. Dyson and M. L. Mehta, Statistical theory of the energy levels of complex systems. iv, *J. Math. Phys.* **4**, 701 (1963).
- [90] E. Bogomolny, R. Dubertrand, and C. Schmit, Spectral statistics of a pseudo-integrable map: the general case, *Nonlinearity* **22**, 2101 (2009).
- [91] E. Bogomolny and C. Schmit, Spectral statistics of a quantum interval-exchange map, *Phys. Rev. Lett.* **93**, 254102 (2004).

Supporting Information for
Shaping Chaos in Bilayer Graphene Cavities

Jucheng Lin,^{1,2,3,*} Yicheng Zhuang,^{1,2,4,*} Anton M.
Graf,^{1,2,5} Joonas Keski-Rahkonen,^{1,2} and Eric J. Heller^{1,2}

¹*Department of Chemistry and Chemical Biology,
Harvard University, Cambridge, Massachusetts 02138, USA*

²*Department of Physics, Harvard University,
Cambridge, Massachusetts 02138, USA*

³*School of Physics and Astronomy,
Shanghai Jiao Tong University, Shanghai 200240, China*

⁴*School of Physics, Peking University, Beijing 100871, China*

⁵*Harvard John A. Paulson School of Engineering and Applied Sciences,
Harvard, Cambridge, Massachusetts 02138, USA*

(Dated: January 5, 2026)

CONTENTS

I. Simulation details	2
A. Scaling method	2
B. Unfolding method	3
C. Sub-sublattice	4
II. Semiclassical ray-dynamics	5
III. Further analysis of eigenstates	7
A. Angle dependence of correlation length	7
B. Momentum space IPR statistics	8
IV. Results of more cases	9
A. Unrotated hexagon with kinks	9
B. Small angle case	11
C. Unsymmetrical case	12
D. Other sizes	13
E. Monolayer graphene case	14
References	16

I. SIMULATION DETAILS

Here, we further describe in detail the methods used in our simulations.

A. Scaling method

We use the scaling method in the tight-binding model [1]. The low-energy continuum Hamiltonian for AB-stacked bilayer graphene in the basis (A_1, B_1, A_2, B_2) is

* These authors contributed equally to this work.

$$H = \begin{pmatrix} \epsilon_{A1} & v\pi^\dagger & -v_4\pi^\dagger & v_3\pi \\ v\pi & \epsilon_{B1} & \gamma_1 & -v_4\pi^\dagger \\ -v_4\pi & \gamma_1 & \epsilon_{A2} & v\pi^\dagger \\ v_3\pi^\dagger & -v_4\pi & v\pi & \epsilon_{B2} \end{pmatrix}, \quad (1)$$

where the effective velocities are

$$v = \frac{\sqrt{3}a\gamma_0}{2\hbar}, \quad v_3 = \frac{\sqrt{3}a\gamma_3}{2\hbar}, \quad v_4 = \frac{\sqrt{3}a\gamma_4}{2\hbar},$$

and the momentum operator is

$$\pi = \xi p_x + i p_y,$$

with $\xi = \pm 1$ for the K and K' valleys.

We employ the scaling method to enlarge the distances between atoms, thereby reducing the total number of atoms in our simulation. The scaled lattice constant is given by $a_s = s a$, where s is the scaling factor and we take $s = 3$ in our work. To preserve the Hamiltonian and the low-energy band structure, the hopping parameters are scaled accordingly:

$$\gamma_{0s} = \frac{\gamma_0}{s}, \quad \gamma_{1s} = \gamma_1, \quad \gamma_{3s} = \frac{\gamma_3}{s}, \quad \gamma_{4s} = \frac{\gamma_4}{s}.$$

B. Unfolding method

To analyze the spectral correlations, we first sort the eigenenergies $\{E_i\}$ in ascending order. The raw spectrum is then unfolded to remove the global variation of the density of states. Specifically, we construct the integrated level counting function $N(E)$ and approximate it by a smooth function $\bar{N}(E)$ obtained from a polynomial fit [2]. The unfolded energies are defined as

$$\varepsilon_i = \bar{N}(E_i), \quad (2)$$

such that the mean level spacing is unity. The nearest-neighbor level spacings are given by

$$s_i = \varepsilon_{i+1} - \varepsilon_i, \quad (3)$$

and are subsequently normalized by their average value. Based on the unfolded spectrum, we compute the nearest-neighbor spacing distribution $P(s)$, the ratio of consecutive spacings $\tilde{r} = \min(s_i, s_{i-1})/\max(s_i, s_{i-1})$, and the spectral rigidity $\Delta_3(L)$ to characterize the spectral statistics.

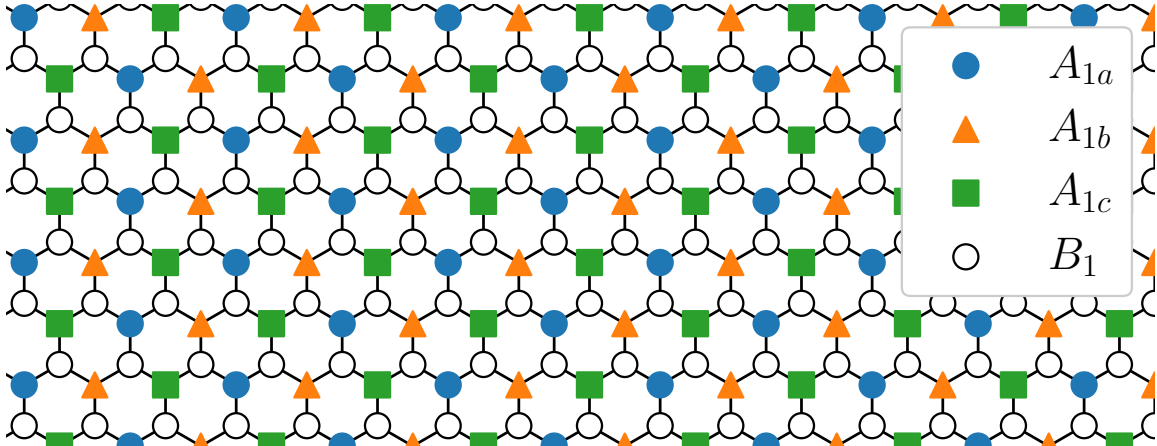


FIG. 1: A diagram showing the sub-sublattice of one layer of BLG

C. Sub-sublattice

In the *Eigenstates* section, we employ the sub-sublattice method to present the real-space probability density distributions of selected eigenstates, following the construction introduced in Ref. [3]. This representation allows us to resolve the spatial structure of the eigenstates in a manner compatible with the valley degrees of freedom of graphene.

The necessity of the sub-sublattice description arises from the fact that graphene eigenstates generally involve contributions from both K and K' valleys. When such states are projected onto a single sublattice, the valley-dependent phase factors lead to rapid oscillations of the wave-function amplitude at the atomic scale. As a result, the probability density defined on the original Bravais lattice exhibits strong site-to-site modulation, obscuring the physically relevant spatial envelope of the eigenstates.

As illustrated in Fig. 1, we now specify how the sub-sublattice decomposition is implemented. We consider the atoms belonging to sublattices A_1 and B_1 in the first graphene layer, and perform the sub-sublattice construction on sublattice A_1 . Along the horizontal direction, three consecutive A_1 atoms are grouped into a single unit, which defines three sub-sublattices denoted as A_{1a} , A_{1b} , and A_{1c} . These three sub-sublattices form a reduced Bravais lattice with primitive vectors

$$\mathbf{a}_{1,\text{sub}} = (3a, 0), \quad \mathbf{a}_{2,\text{sub}} = (\sqrt{3}a, 0). \quad (4)$$

With this construction, the probability density defined on each sub-sublattice becomes continuous in real space.

To make explicit why this construction removes the atomic-scale oscillations discussed above, we consider a single wave vector \mathbf{k} contributing to the wave function on sublattice A_1 ,

$$|\psi^{\mathbf{k}}\rangle_{A_1} = \frac{1}{\sqrt{N}} \sum_{n,m} \exp(i \mathbf{k} \cdot \mathbf{R}_{nm}) |n, m\rangle. \quad (5)$$

The position vector of an A_1 -sublattice site is defined as

$$\mathbf{R}_{nm} \equiv |n, m\rangle = n \mathbf{a}_1 + m \mathbf{a}_2, \quad (6)$$

where n and m are integers, and $\mathbf{a}_1 = (a, 0)$ and $\mathbf{a}_2 = (\frac{1}{2}a, \frac{\sqrt{3}}{2}a)$ are the primitive Bravais lattice vectors.

The two inequivalent valleys are located at

$$\mathbf{K} = \left(\frac{4\pi}{3a}, 0 \right), \quad \mathbf{K}' = \left(-\frac{4\pi}{3a}, 0 \right). \quad (7)$$

Substituting the valley wave vectors into the expression above yields

$$|\psi^{K(K')}\rangle_{A_1} = \frac{1}{\sqrt{N}} \sum_{n,m} \exp\left[(-) \frac{2\pi i}{3} (2n + m)\right] |n, m\rangle. \quad (8)$$

The phase factor $\exp[(-) 2\pi i(2n + m)/3]$ can take only three distinct values, which are identical for all sites belonging to the same sub-sublattice, as illustrated in Fig. 1. Consequently, translational symmetry is restored within each sub-sublattice provided that the primitive translation vectors are chosen as $\mathbf{a}_{1,\text{sub}} = (3a, 0)$ and $\mathbf{a}_{2,\text{sub}} = (\sqrt{3}a, 0)$.

II. SEMICLASSICAL RAY-DYNAMICS

Our semiclassical ray construction is formulated in momentum space and is controlled by the Fermi contour together with the associated group velocity. Throughout this work we base the ray dynamics on the standard four-band continuum description of AB-stacked bilayer graphene ((1)). In particular, the trigonal-warping anisotropy that drives the nontrivial ray deflection originates from the γ_3 term.

To implement the warped reflection law quantitatively at the energies studied here (e.g., $E_F \simeq 0.2$ eV), we construct a numerical Fermi contour using the standard AB-stacked tight-binding parameters ($t_0 = 3.16$ eV, $t_1 = 0.381$ eV, $t_3 = 0.38$ eV, $t_4 = 0.14$ eV, and lattice constant $a = 0.24595$ nm), and evaluate the group velocity $\mathbf{v}(\mathbf{k}) = \nabla_{\mathbf{k}} E(\mathbf{k})$ along this contour. In this regime the contour is a single closed, approximately convex curve.

For a wave packet confined to a single band $E(\mathbf{k})$ in a static scalar potential $V(\mathbf{r})$, the semiclassical equations of motion are

$$\dot{\mathbf{r}} = \nabla_{\mathbf{k}}E(\mathbf{k}) - \dot{\mathbf{k}} \times \boldsymbol{\Omega}(\mathbf{k}), \quad \hbar\dot{\mathbf{k}} = -\nabla_{\mathbf{r}}V(\mathbf{r}), \quad (9)$$

where $\boldsymbol{\Omega}(\mathbf{k})$ is the Berry curvature. Because BLG at low energy is gapless, $\boldsymbol{\Omega}(\mathbf{k}) = 0$, and no anomalous velocity term appears [4].

Thus all semiclassical structure arises from the strongly anisotropic group velocity $\mathbf{v}(\mathbf{k}) = \nabla_{\mathbf{k}}E(\mathbf{k})$.

During free flight the band energy is conserved. When a ray encounters a hard wall with outward normal $\hat{\mathbf{n}}$, the reflected momentum \mathbf{k}' must satisfy

$$E(\mathbf{k}') = E(\mathbf{k}), \quad \mathbf{k}' \cdot \hat{\mathbf{t}} = \mathbf{k} \cdot \hat{\mathbf{t}}. \quad (10)$$

Equivalently, writing $\mathbf{k} = k_t\hat{\mathbf{t}} + k_n\hat{\mathbf{n}}$ with $\hat{\mathbf{t}} = \hat{\mathbf{z}} \times \hat{\mathbf{n}}$, the tangential component k_t is preserved, while k'_n is determined from energy conservation along with the flipped normal velocity [5].

Implementing the semiclassical dynamics of a warped-dispersion billiard in a polygonal cavity is numerically difficult. The regular hexagon is a pseudointegrable billiard whose dynamics is singular at the corners: most of the boundary is flat, while the vertices act as isolated singular points. In a direct ray-propagation scheme based on continuous time evolution and local boundary reflection, trajectories can suffer from severe numerical instabilities, including *grazing reflections* and *spurious trapping near corners*. Near a vertex, the result can depend on how the corner is handled. Physically, exact vertex hits occur only for a measure-zero set of initial conditions; for generic trajectories, collisions always occur on the interior of an edge, arbitrarily close to a corner if needed. Resolving this behavior accurately requires very fine time steps and careful corner handling, which becomes inefficient and unstable for long trajectories.

To overcome these difficulties, we rewrite the dynamics as a discrete mapping between successive boundary collisions. We tabulate the relation between the incidence angle φ_{in} and the outgoing angle φ_{out} , determined by conservation of energy and tangential component k_t . Each table contains about $1 \times 10^5 - 3 \times 10^5$ sampled angles. This approach encodes the warped reflection law once and for all, and removes the need to solve for φ_{out} by a local root search at every collision.

Between collisions, the next collision point is found by ray-boundary intersection. The dynamics is thus an alternation of (i) intersection updates for free flight and (ii) table-based

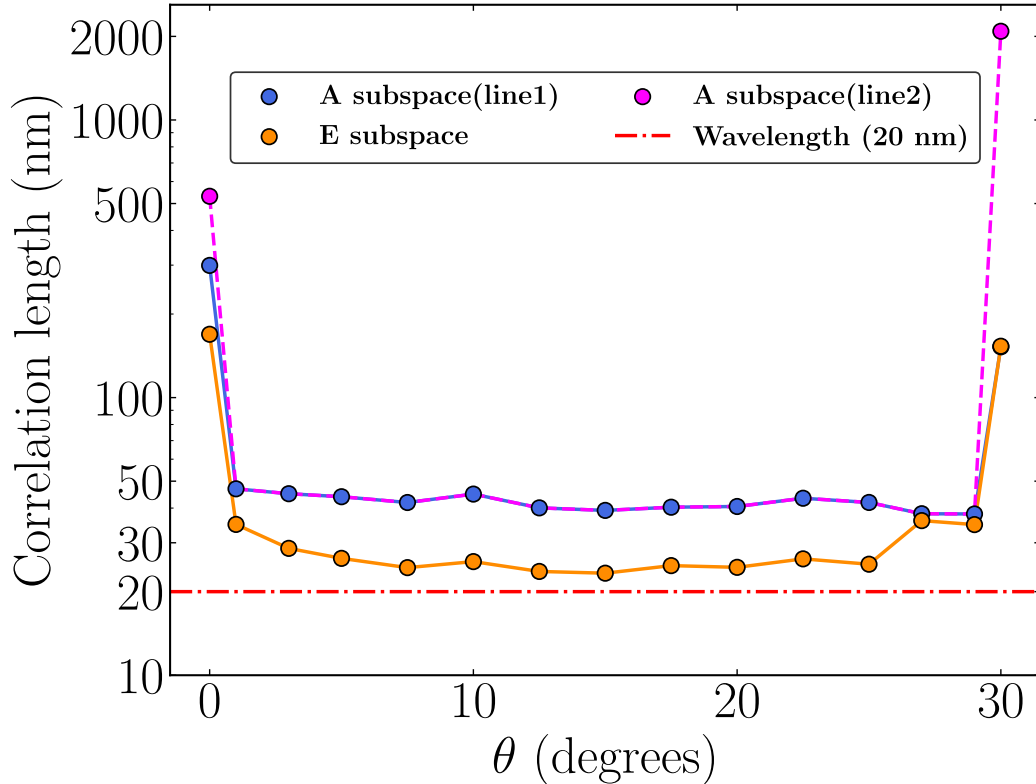


FIG. 2: Angle dependence of the correlation length on the rotation angle θ for the A and E subspaces. In the A subspaces, two curves are plotted. The blue solid curve corresponds to the pseudointegrable sector at $\theta = 0^\circ$ and 30° for the unrotated cavities, while the purple dashed curve denotes the integrable one.

updates for reflection. This map-based scheme keeps high angular accuracy even for nearly grazing trajectories, and avoids artificial corner sticking and other corner-related numerical artifacts. As a result, we can compute long trajectories and Poincaré sections robustly.

III. FURTHER ANALYSIS OF EIGENSTATES

A. Angle dependence of correlation length

Fig. 2 summarizes the dependence of the average correlation length on the rotation angle θ for different symmetry subspaces. In all cases, the correlation length rapidly decreases toward the wavelength scale upon rotation. This trend further supports the conclusion

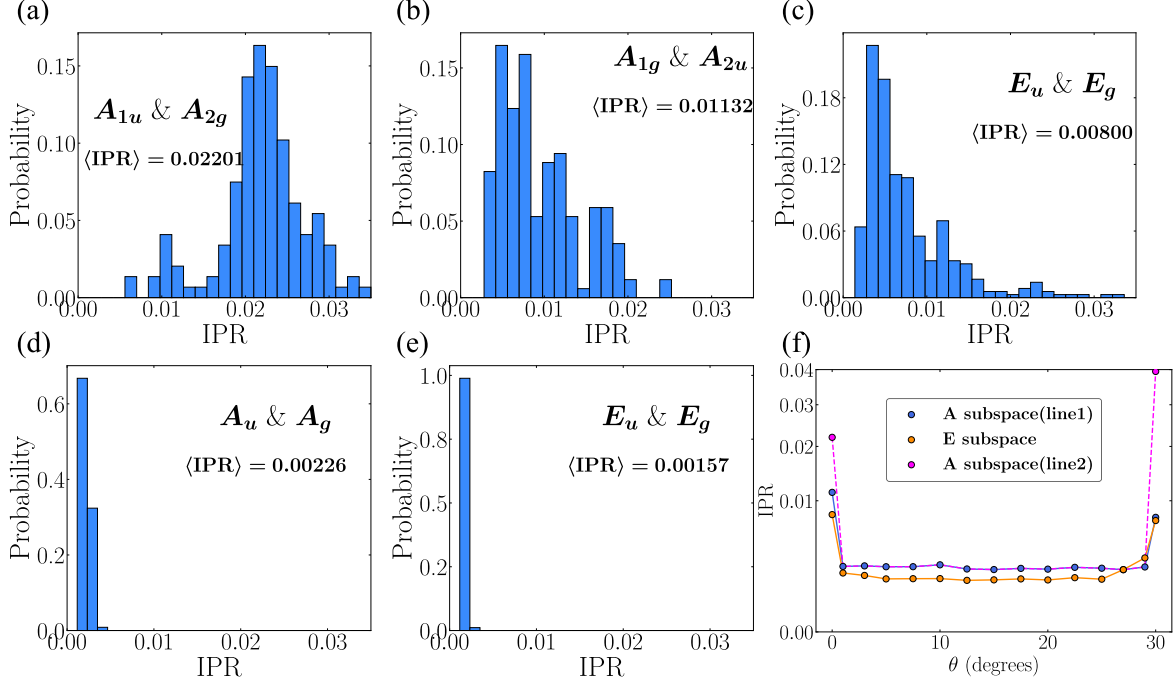


FIG. 3: IPR of momentum space analysis for eigenstates. (a,b,c) Statistics of the IPR in momentum space for the eigenstates of unrotated cavities across different subspaces. (d,e) The corresponding results for rotated cavities. (f) The angle dependence of the IPR on the rotation angle θ for the A and E subspaces, where the second line of the A subspace starts and ends in the integrable sectors at $\theta = 0^\circ$ and $\theta = 30^\circ$.

that misalignment between the lattice and the cavity boundary drives the system from a pseudointegrable regime to one exhibiting fully developed quantum-chaotic behavior.

B. Momentum space IPR statistics

We further introduce an additional measure to illustrate how rotation drives the wavefunctions toward a Berry-wave-like structure. Specifically, we examine the number of plane waves composing each wavefunction, which can be quantified by the degree of localization in momentum space. Accordingly, we compute the inverse participation ratio (IPR) of the momentum-space density distribution $|\tilde{\psi}(\mathbf{k})|^2$, defined as

$$\text{IPR} = \frac{\sum_{\mathbf{k}} |\tilde{\psi}(\mathbf{k})|^4}{\left(\sum_{\mathbf{k}} |\tilde{\psi}(\mathbf{k})|^2\right)^2}.$$

A larger IPR indicates stronger localization in momentum space, corresponding to fewer plane-wave components contributing to the wavefunction.

For both unrotated and rotated cavities, we select a total of 1,056 eigenstates near 0.2 eV and perform statistical analysis of each symmetry subspace based on their momentum-space IPR. Fig. 3(a)-(c) show the IPR distribution for eigenstates of the unrotated cavity, while Fig. 3(d) and (e) present the corresponding results for rotated cavities with a rotation angle of $\theta = 15^\circ$, with the average IPR indicated. We observe that the IPR decreases significantly, with only a small variance in the IPR distribution upon rotation. Fig. 3(f) summarizes the angle dependence of the average IPR, showing that the reduced IPR relative to the unrotated case is robust against changes in rotation angle. These results indicate that upon rotation, the wavefunctions consist of a larger number of plane wave components with different momenta, reflecting an increased degree of chaotic behavior.

IV. RESULTS OF MORE CASES

A. Unrotated hexagon with kinks

In addition to the ergodicity of the classical dynamics in the rotated hexagon, edge roughness constitutes another important ingredient that must be taken into account. To disentangle the roles of these two factors in producing quantum chaotic behavior, we consider a reference system in which kinks are introduced into an unrotated hexagon while preserving the S_6 symmetry. This system shares the same symmetry and comparable edge roughness with the rotated hexagon, but differs in its underlying classical dynamical correspondence. Consequently, the difference observed in their quantum chaotic behavior can be attributed to the trigonal-warping-induced modification of the classical dynamics.

In Fig. 4(a), we show a hexagon rotated by an angle $\theta = 1^\circ$. The inset displays the atomic-scale edge profile, revealing detailed boundary structures. A mixture of zigzag and armchair terminations is observed; in particular, a representative turning point corresponding to an armchair edge is highlighted by a red box, which is a *kink*. In Fig. 4(b), we introduce the same type of armchair-edge kinks along the boundary of an unrotated hexagon while preserving the S_6 symmetry.

We count the number of armchair-edge kinks and denote it by n ; for reference, $n = 11$ for

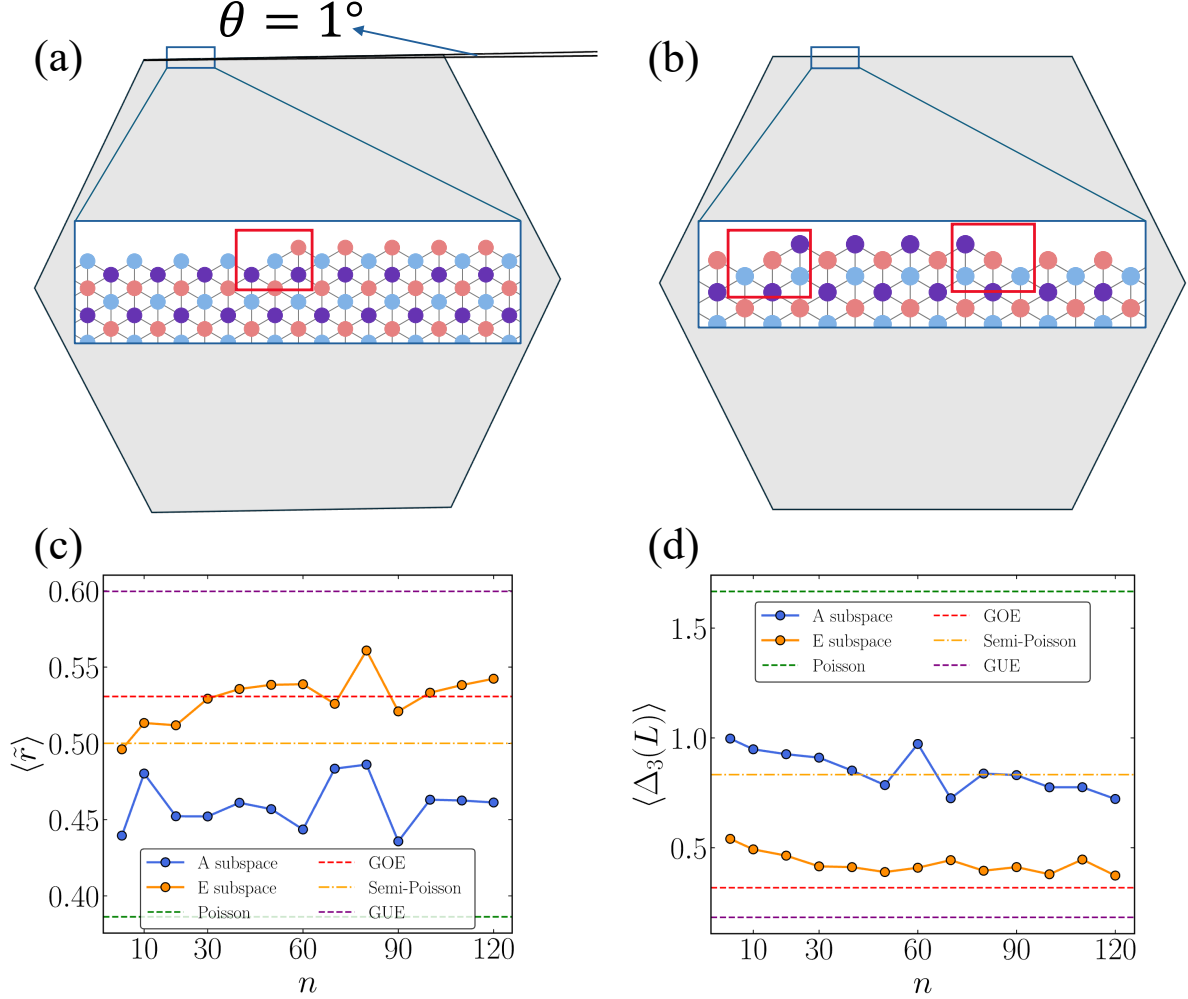


FIG. 4: Atomic geometry of the rotated cavities and unrotated cavities with kinks, the dependence of $\langle \tilde{r} \rangle$ and $\langle \Delta_3(L) \rangle$ on kinks number (a) Rotated hexagon with a small rotation angle ($\theta = 1^\circ$); the inset shows the atomic profile at the cavity edge, with armchair edges highlighted in red and the remaining edges zigzag. (b) Unrotated hexagon with artificial edge disorder, red boxes indicate armchair edges. (c,d) Dependence of $\langle \tilde{r} \rangle$ (c) and $\langle \Delta_3(L) \rangle$ (d) on the number of added armchair kinks n , for the S_6 symmetry group.

$\theta = 1^\circ$, and n follows an approximately $\sin \theta$ -dependent scaling. We then perform numerical simulations to investigate how the level spacing statistics evolve with increasing kink number. Fig. 4(c) shows the behavior of $\langle \tilde{r} \rangle$. We find that the A sectors remain at an intermediate value between the GOE and Poisson statistics, indicating the persistence of pseudointegrable behavior in this system. In contrast, the E sectors exhibit an increasing $\langle \tilde{r} \rangle$ as more kinks are introduced. Nevertheless, even for large n , $\langle \tilde{r} \rangle$ does not reach the level of chaoticity observed

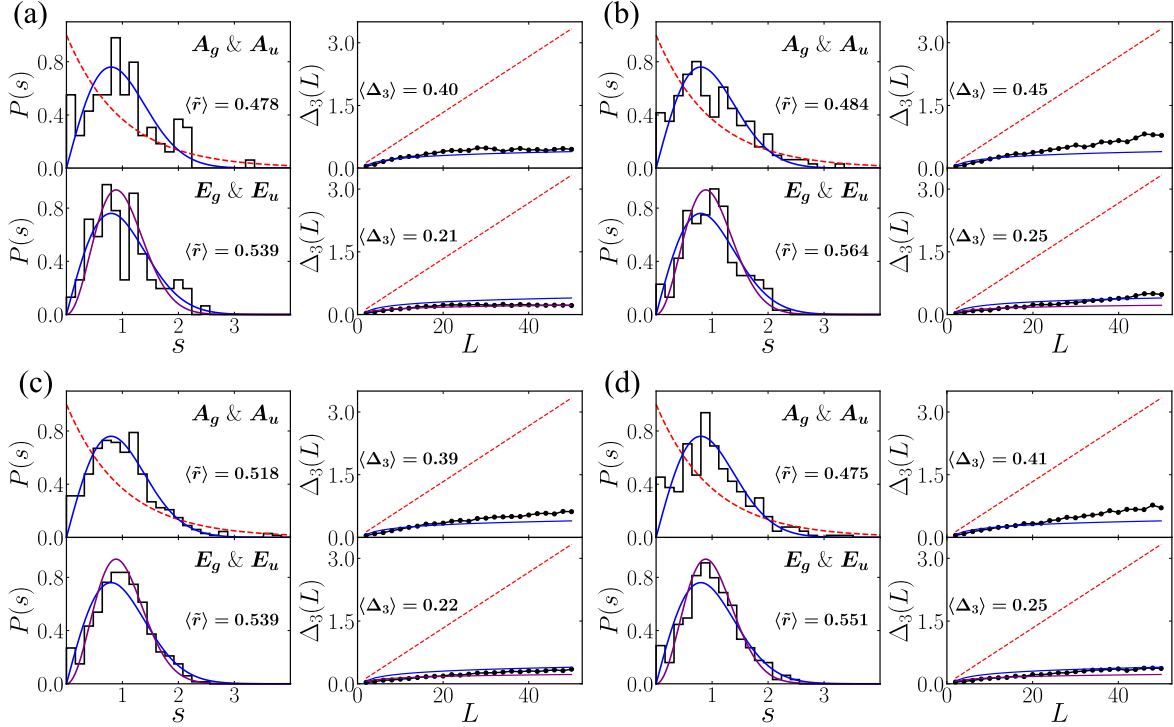


FIG. 5: The figures illustrate the level spacing distributions and spectral rigidity for the small-angle cases, with the average r value $\langle \tilde{r} \rangle$ and average rigidity $\langle \Delta_3(L) \rangle$ indicated. The results correspond to rotation angles θ of (a) 0.1° , (b) 0.2° , (c) 0.3° , and (d) 0.4° . The red dashed line denotes the Poisson distribution, the blue solid line represents the Wigner–Dyson distribution for the GOE, and the purple solid line represents the Wigner–Dyson distribution for the GUE.

in the rotated hexagon, where it remains robustly between the GOE and GUE values over a wide range of rotation angles. Fig. 4(d) shows the behavior of the spectral rigidity $\langle \Delta_3(L) \rangle$. A similar trend is observed: the A sectors remain at an intermediate value, while the E sectors approach the GOE prediction instead of GUE prediction as in the rotated hexagon.

B. Small angle case

To illustrate the sensitivity of rotational effects on quantum chaotic behavior, we present four small angle cases with $\theta = 0.1^\circ, 0.2^\circ, 0.3^\circ$, and 0.4° in Fig. 5, showing both the level spacing distribution and spectral rigidity for the A and E sectors. Even at these small angles, the A subspaces exhibit a semi-Poisson level spacing distribution with $\langle \tilde{r} \rangle$ between

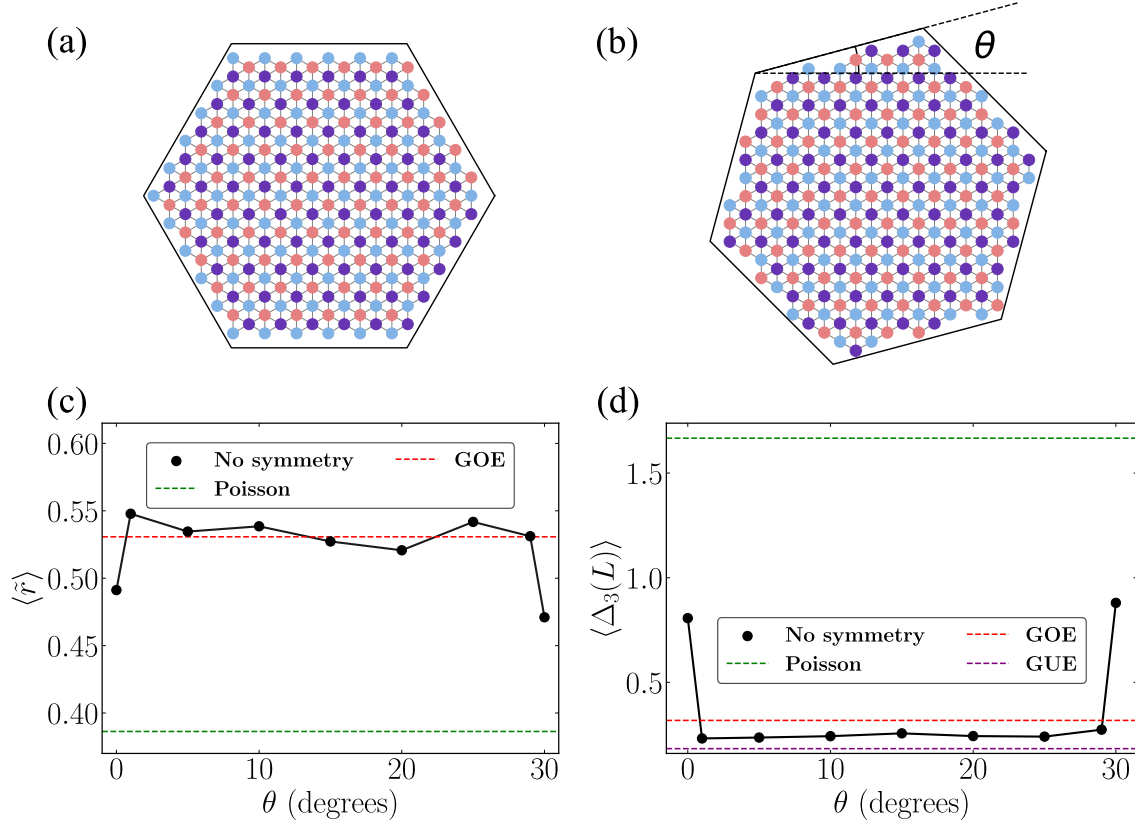


FIG. 6: Atomic geometries of rotated and unrotated symmetry-broken BLG cavities, and the angle dependence of $\langle \tilde{r} \rangle$ and $\langle \Delta_3(L) \rangle$ on the rotation angle θ . (a) Atomic profile of an unrotated hexagon, exhibiting no symmetry. (b) Corresponding profile for the rotated hexagon, which also lacks symmetry. (c) Dependence of $\langle \tilde{r} \rangle$ on the rotation angle θ . (d) Dependence of $\langle \Delta_3(L) \rangle$ on the rotation angle θ .

$\langle \tilde{r} \rangle_{\text{Poisson}} = 0.386$ and $\langle \tilde{r} \rangle_{\text{GOE}} = 0.531$, whereas the E subspaces display an intermediate distribution between GOE and GUE, with $\langle \tilde{r} \rangle$ between $\langle \tilde{r} \rangle_{\text{GOE}} = 0.531$ and $\langle \tilde{r} \rangle_{\text{GUE}} = 0.600$. In addition, the spectral rigidity exhibits signatures of chaotic behavior in both subspaces. For the A subspaces, the rigidity closely follows the GOE prediction, whereas for the E subspaces, it falls between the GOE and GUE predictions.

C. Unsymmetrical case

We present another example of BLG cavities without point-group symmetry. By shifting the hexagonal boundaries, the atomic point-group symmetry is broken in both the unrotated

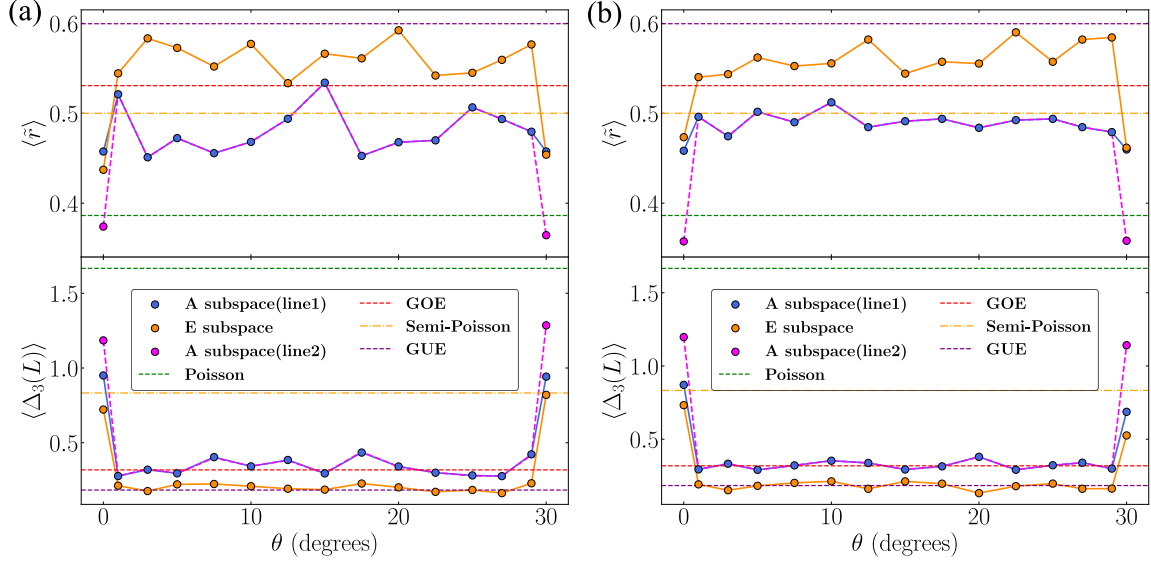


FIG. 7: The figures illustrate the dependence of $\langle \tilde{r} \rangle$ and $\langle \Delta_3(L) \rangle$ on the rotation angle θ for cavities of different sizes: (a) $r = 450$ nm, (b) $r = 500$ nm.

and rotated cavities, as shown in Fig. 6(a) and (b). For this type of cavity, we perform the eigenenergy analysis in the full Hilbert space without symmetry decomposition.

The angle dependence of $\langle \tilde{r} \rangle$ as a function of the rotation angle θ , shown in Fig. 6(c), reveals a transition of $\langle \tilde{r} \rangle$ from an intermediate value in the unrotated cases at $\theta = 0^\circ$ and $\theta = 30^\circ$ to a value close to the GOE prediction upon rotation. The intermediate values of $\langle \tilde{r} \rangle$ for the unrotated cavities reflect the pseudointegrable nature of the hexagonal geometry, whereas the values of $\langle \tilde{r} \rangle$ observed in the rotated cavities approaching GOE prediction indicate the emergence of quantum chaotic behavior induced by rotation.

A similar trend is observed in the angle dependence of $\langle \Delta_3(L) \rangle$, as shown in Fig. 6(d). Specifically, $\langle \Delta_3(L) \rangle$ remains at an intermediate value for the unrotated cavities, while for the rotated cavities it takes values between the GOE and GUE predictions.

D. Other sizes

To rule out the possibility that the results presented in the main text arise from a special cavity size, we perform level statistics analyses for BLG cavities with other radii, $r = 450$ nm and $r = 500$ nm. The angle dependence of $\langle \tilde{r} \rangle$ and $\langle \Delta_3(L) \rangle$ for different symmetry subspaces, shown in Fig. 7, exhibits the same qualitative transition upon rotation.

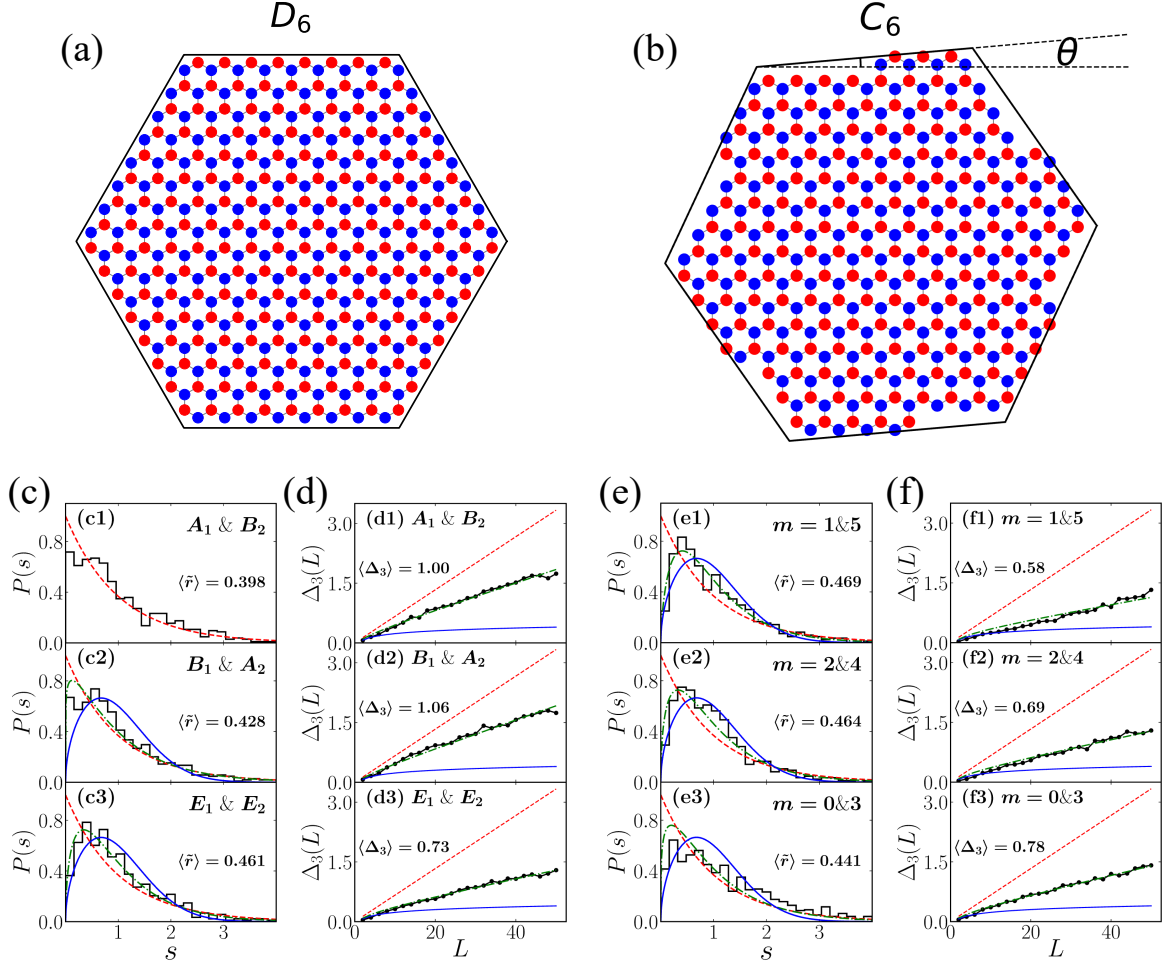


FIG. 8: Atomic geometries of rotated and unrotated MLG cavities and the corresponding level statistics results. (a) Atomic configuration of an unrotated hexagonal MLG cavity exhibiting D_6 symmetry. (b) Atomic configuration of a rotated hexagonal MLG cavity with a rotation angle $\theta = 5^\circ$, exhibiting C_6 symmetry. (c,d) Nearest-neighbor level-spacing distribution and spectral rigidity for the unrotated MLG cavities. (e,f) Corresponding results to panels (c) and (d) for the rotated MLG cavities with $\theta = 5^\circ$.

E. Monolayer graphene case

In contrast to bilayer graphene cavities, we also investigate the quantum chaotic behavior of monolayer graphene (MLG) cavities.

The unrotated MLG cavity preserves D_6 symmetry, as shown in Fig. 8(a), while the rotated cavity preserves C_6 symmetry, as shown in Fig. 8(b). The eigenstates of the cavity can be classified according to the irreducible representations of the corresponding point

TABLE I: Subspace decomposition of the MLG cavity according to point group symmetries.

(a) D_6 symmetry				(b) C_6 symmetry		
Irrep	σ	m	Dim	Irrep	m	Dim
A_1	+1	0	1	ρ_0	0	1
A_2	-1	0	1	ρ_1	1	1
B_1	+1	3	1	ρ_2	2	1
B_2	-1	3	1	ρ_3	3	1
E_1	0	1, 5	2	ρ_4	4	1
E_2	0	2, 4	2	ρ_5	5	1

group. The symmetry decomposition of the Hilbert space is determined by the rotational and mirror symmetries. The six-fold rotation operator C_6 acts on the lattice sites and has eigenvalues

$$\lambda_m = e^{i2\pi m/6}, \quad m = 0, 1, 2, 3, 4, 5, \quad (11)$$

which define the rotation quantum number m of each subspace. The mirror (reflection) operator σ acts along a symmetry axis of the hexagon and has eigenvalues $\sigma = \pm 1$. Each irreducible subspace of the Hilbert space can thus be labeled by the pair (m, σ) .

For the unrotated cavity with D_6 symmetry, both rotation and mirror symmetries are preserved, and the Hilbert space is decomposed into the subspaces A_1, A_2, B_1, B_2, E_1 and E_2 , with the corresponding m and σ values indicated in Table I. For the rotated cavity with C_6 symmetry, only the six-fold rotation is preserved, and the Hilbert space is decomposed into six one-dimensional subspaces ρ_0, \dots, ρ_5 , labeled by the rotation quantum number $m = 0, 1, \dots, 5$; mirror symmetry σ is no longer relevant. The full subspace labeling for both symmetries is summarized in Table I.

Based on the symmetry analysis of the MLG cavities, we perform level statistics calculations for the unrotated cavities, as shown in Fig. 8(c) and (d). In Fig. 8(c), the nearest-neighbor level spacing distributions for the A_1 and B_2 sectors follow the Poisson distribution,

whereas the B_1 and A_2 sectors, as well as the two two-dimensional E sectors, exhibit semi-Poisson statistics. Correspondingly, the spectral rigidity for all subspaces, shown in Fig. 8(d), is well described by the semi-Poisson fit.

For the rotated cavities, the same level statistics analysis is performed, as shown in Fig. 8(e) and (f). Because of the approximate mirror symmetry of the rotated MLG cavity, we remove the near-zero level spacings associated with the nearly degenerate pairs in the $m = 0$ and $m = 3$ sectors. Here, all subspaces display semi-Poisson statistics in the nearest-neighbor level spacing distributions (Fig. 8(e)), and the corresponding spectral rigidity (Fig. 8(f)) is also consistent with the semi-Poisson fit.

Further results show that these results show that rotation does not drive MLG cavities toward quantum chaos; the rotated BLG cavities still preserve the pseudointegrability of the classical limit and exhibit semi-Poisson level statistics. This behavior arises from the isotropic Fermi surface of MLG cavities, in contrast to the trigonal-warped Fermi surface in BLG cavities. These findings further justify the choice of BLG cavities as the platform for our study.

-
- [1] M.-H. Liu, P. Rickhaus, P. Makk, E. Tóvári, R. Maurand, F. Tkatschenko, M. Weiss, C. Schönenberger, and K. Richter, Scalable tight-binding model for graphene, *Phys. Rev. Lett.* **114**, 036601 (2015).
 - [2] A. A. Abul-Magd and A. Y. Abul-Magd, Unfolding of the spectrum for chaotic and mixed systems, *Physica A: Stat. Mech. Appl.* **396**, 185–194 (2014).
 - [3] D. P. Żebrowski, E. Wach, and B. Szafran, Confined states in quantum dots defined within finite flakes of bilayer graphene: Coupling to the edge, ionization threshold, and valley degeneracy, *Phys. Rev. B* **88**, 165405 (2013).
 - [4] G. Sundaram and Q. Niu, Wave-packet dynamics in slowly perturbed crystals: Gradient corrections and berry-phase effects, *Phys. Rev. B* **59**, 14915 (1999).
 - [5] L. Seemann, A. Knothe, and M. Hentschel, Gate-tunable regular and chaotic electron dynamics in ballistic bilayer graphene cavities, *Phys. Rev. B* **107**, 205404 (2023).